The effects of kelp canopy submersion on the remote sensing of surface-canopy forming kelps

By

Brian D. Timmer

B.Sc. Vancouver Island University, 2019

A Thesis Submitted in Partial Fulfilment of the Requirements for the

Degree of

MASTER OF SCIENCE

in the Department of Geography

We acknowledge and respect the lək^{w}əŋən peoples on whose traditional territory the university stands and the Songhees, Esquimalt and W̱SÁNEĆ peoples whose historical relationships with the land continue to this day.

The effects of kelp canopy submersion on the remote sensing of surface-canopy forming kelps

By

Brian D. Timmer

B.Sc. Vancouver Island University, 2019

Supervisory Committee:

Dr. M. Costa, Co-supervisor (Department of Geography)

Dr. F. Juanes, Co-supervisor (Department of Biology)

Dr. M. Hessing-Lewis, Committee Member (Hakai Institute)

Abstract

Kelp forests are highly productive three-dimensional marine ecosystems that provide valuable ecosystem services globally. Along the coast of British Columbia, *Macrocystis pyrifera* and *Nereocystis luetkeana* are two key species that form surface-canopies that are vulnerable to both biotic and abiotic drivers; making it imperative to monitor and understand whether these ecosystems are changing in the face of climate change. The monitoring of kelp forests is commonly enhanced by use of remote sensing, which allows researchers to survey large portions of the coast where it would otherwise be difficult to collect data, and to use archived imagery for comparisons of historic and contemporary kelp forest trends. Generally, the remote sensing of kelp surface-canopy relies on differences in the high near-infrared (NIR; 700-1000 nm) signal of kelp and the low NIR signal of water. However, kelp surface-canopy reflectance signals can be affected by submergence under water, caused by oceanographic features like tides and currents, or simply due to differences in the morphology and buoyancy of kelp canopy structures. This submersion may cause uncertainties when estimating the surface-canopy area of kelp beds in remote sensing imagery. This research aims to understand the effects of submersion on the remote sensing of kelp surface-canopy. To address our goal, (i) *Nereocystis* canopy structures (bulb and blade) were submerged while collecting above-water hyperspectral measurements. The hyperspectral data into the bandwidths of high-resolution multispectral aerial and space-borne sensors and vegetation indices were calculated to understand the kelp detection limits when using shorter red-edge wavelengths (RE; 690-750 nm) instead of the longer NIR wavelengths. The results showed that submerged kelp can be detected deeper in the water column using shorter RE wavelengths compared to the more commonly used NIR wavelengths. Further, (ii) *in situ* hyperspectral data were also collected for the different surface-canopy structures and

compared with UAV imagery, which showed that the buoyancy of the kelp canopy structures at the surface affected the relative magnitude of reflectance in both the RE and NIR and supported the findings of the submersion experiment. The total surface-canopy area derived from classification with both RE and NIR vegetation indices were compared in the UAV imagery, and the RE index detected roughly 18% more kelp than the NIR index, with no differences seen between *Macrocystis* and *Nereocystis*, or between high and low tide in beds larger than 150m^2. Finally, (iii) to understand how submersion by tides and currents affect the ability to estimate surface-canopy area for both *Macrocystis* and *Nereocystis*, surface-canopy area was derived from multispectral unoccupied aerial vehicle (UAV) imagery and compared with *in situ* tide and current data, which showed that surface-canopy area had a strong negative linear relationship with tidal height at all sites regardless of species. *Macrocystis* occupied sites where currents were low (<10cm/s) and did not affect the surface-canopy. Therefore, the extent of all *Macrocystis* beds decreased at a similar rate over their tidal range (22.7 $\pm$ 2.8%/m). *Nereocystis* beds occupied a wider range of current speeds (0.0 - 19.0 cm/s), and at sites with high current speeds (> 10 cm/s) increasing current and tidal height decreased surface-canopy area simultaneously, resulting in both a higher and more variable rate of decrease (30.5 $\pm$ 9.1%/m) with increasing tidal height than *Macrocystis*. Together, this thesis addressed critical questions related to the effects of kelp submersion on the remote sensing of surface-canopy forming kelps, and we provide recommendation for remote sensors who wish to minimize errors when using remote sensing to map kelp forests.

Table of Contents

List of Tables

List of Figures

Acknowledgements

I would like to thank my supervisory committee – Dr. Maycira Costa, Dr. Francis Juanes, and Dr. Margot Hessing-Lewis for their support and guidance throughout this thesis. I would also like to thank all of the collaborators on this project, including the Hakai Institute and especially Luba Reshitnyk for being an amazing mentor, and for providing her knowledge, skills, and leadership with field work, experiments, data processing, and just being an all around really nice person. Many thanks to Lianna Gendall for helping with field work as well as being a good friend over the past couple of years. Thank you to all my colleagues in the Spectral lab, especially Alejandra, Vishnu, and Nicola for providing support, guidance, and encouragement throughout my master's studies. Finally, I would like to thank my wife Sarah, my family members, and my friends for their support and patience as I disappeared for days or weeks at a time while working on this thesis.

1.0 Introduction

1.1 Overview

Kelp forests (order Laminariales) are found in temperate and Arctic seas worldwide, forming biogenic canopies that act as habitat for numerous creatures while also supporting primary production and magnifying secondary production in nearshore ecosystems (Duggins *et al.*, 1989; Krumhansl *et al.*, 2016; Wernberg *et al.*, 2019). In the Northeast Pacific, the largest kelp species are the surface-canopy forming kelps, *Macrocystis pyrifera* (giant kelp) and *Nereocystis luetkeana* (bull kelp), both of which have buoyant gas bladders that raise their canopy from the sea-floor to the ocean's surface to maximise photosynthesis (Nicholson, 1970; Druehl & Wheeler, 1986). Given their importance, there has been a push in recent years to monitor the status of kelp forests (Krumhansl *et al.*, 2016; Schroeder *et al.*, 2019a; Hamilton *et al.*, 2020; Bell *et al.*, 2020; Cavanaugh *et al.*, 2021a), with multiple studies finding that surface-canopy forming kelps have declined and even been extirpated in some regions due to extreme warming events (Tegner & Dayton, 1987; Cavanaugh *et al.*, 2011) and overgrazing as a result of ecological regime shifts (Rogers-Bennett & Catton, 2019). However, some kelp forests remain stable, or are recovering from previous declines (Krumhansl *et al.*, 2016; Mora-Soto *et al.*, 2020), making it important to continue monitoring these vital ecosystems.

Remote sensing techniques have been used to monitor and track changes in surface-canopy forming kelps of the Northeast Pacific for over half of a century, with methods that generally focus on detecting the high near-infrared signal (700-1000 nm) that reflects from of the surface-canopy in contrast with the low near-infrared signal of water (Jensen, 1980; Sutherland, 2008). Modern remote sensors use satellites, occupied airborne systems, and unoccupied airborne systems to monitor kelp forests, with spatial, spectral, and temporal trade-offs for imagery

acquisition between sensors from each type of system (Schroeder *et al.*, 2019b; Cavanaugh *et al.*, 2021a). For instance, on the outer-coast between California and Washington State, kelp forest monitoring has mainly focused on large, monospecific, offshore beds, and free historical imagery acquired by the Landsat satellite series has been used to assess changes over time, ranging back to the 1980s (Hamilton *et al.*, 2020; Bell *et al.*, 2020). With imagery time series, it is important to consider the tidal height during imagery acquisition because increases in tidal height can submerge surface-canopy, causing underestimates of surface-canopy area (Britton-Simmons *et al.*, 2008; Cavanaugh *et al.*, 2021b). Users generally mitigate the uncertainties related to changes in tidal height by selecting (or planning) imagery acquired during low tides when the majority of kelp canopy is at the surface (Pfister *et al.*, 2017; Schroeder *et al.*, 2019a; Hamilton *et al.*, 2020; Bell *et al.*, 2020).

The availability of quality low-tide kelp forest imagery may be reduced due to multiple factors when moving northward towards British Columbia and Alaska. For instance, both the tidal range and the frequency of cloudy days generally increase northward along the Pacific coastline (Stekoll *et al.*, 2006; Cavanaugh *et al.*, 2021a), which can reduce the availability of low-tide kelp forest imagery (Stekoll *et al.*, 2006). In addition, the coastline becomes much more complex with thousands of islands and inlets, and kelp often grows in a thin fringe along the shorelines making it difficult to use lower-spatial resolution (10-30 m) sensors for kelp detection (Nijland *et al.*, 2019; Schroeder *et al.*, 2019a). Yet another complicating factor is that the complex coastline facilitates a mix of *Macrocystis* and *Nereocystis* habitat, sometimes even in mixed beds (Sutherland, 2008). Although there are known differences in morphology between *Macrocystis* fronds and *Nereocystis* bulbs and blades, most remote sensing studies only focus on a single species (Schroeder *et al.*, 2019b; Hamilton *et al.*, 2020; Bell *et al.*, 2020; Butler *et al.*, 2020) or

do not differentiate between the two (Nijland *et al.*, 2019; Mora-Soto *et al.*, 2020). Therefore, there has been little focus on defining how differences in buoyancy between surface-canopy structures or rates of submersion might lead to above-water reflectance differences between *Macrocystis* and *Nereocystis* at a given tidal stage (Schroeder *et al.*, 2019b; Cavanaugh *et al.*, 2021b).

1.2 Research Objectives

The goal of this thesis is to understand how submersion of kelp canopy affects the above-water reflectance of surface-canopy forming kelps, with a focus on better understanding how submersion due to tides, currents, and morphology affect the estimation of surface-canopy area for both *Macrocystis pyrifera* and *Nereocystis luetkeana*. To address this goal, the following objectives were defined:

(1) Document the effects of submersion on the above-water reflectance and the detection limits of kelp, focusing on *Nereocystis* bulb and blades;

(2) Characterize how morphological differences between *Nereocystis* and *Macrocystis* surface-canopy structures affect the *in situ* above-water spectral signal; and

(3) Investigate the effects of submersion by tides and currents on the estimated surface-canopy area of *Nereocystis* and *Macrocystis* in high-resolution multispectral UAV imagery.

1.3 Thesis Structure

This thesis is divided into two separate papers to address the research objectives. The first paper (chapter 2) demonstrates how submersion of *Nereocystis* surface-canopy changes its above-water

hyperspectral signature, and how differences in band selection for kelp classification result in different depth detection limits for both *Nereocystis* bulbs and blades. The second paper (Chapter 3) details the effects of tides and currents on *Macrocystis* and *Nereocystis* surface-canopy area in high-resolution multispectral UAV imagery. Chapter 3 also addresses *in situ* hyperspectral data to better understand differences seen between species in the imagery. These papers are planned as independent publications, and therefore, there are some overlapping points regarding the remote sensing of kelp forests. The summary and conclusion (Chapter 4) address the key findings from both papers.

2.0 Comparing the Use of Red-edge and Near-infrared Wavelengths for Detecting Submerged Kelp Canopy.

2.1 Abstract

Kelp forests are commonly classified within remote sensing imagery by contrasting the high reflectance in the near-infrared spectral region of kelp canopy floating at the surface with the low reflectance in the same spectral region of water. However, kelp canopy is often submerged below the surface of the water, making it important to understand the effects of kelp submersion on the above-water reflectance of kelp, and the depth to which kelp can be detected, in order to reduce uncertainties around the kelp canopy area when mapping kelp. Here, we characterized changes to the above-water spectra of *Nereocystis luetkeana* (Bull kelp) as different canopy structures (bulb and blades) were submerged in water from the surface to 100 cm in 10 cm increments, while collecting above-water hyperspectral measurements with a spectroradiometer (325–1075 nm). The hyperspectral data were simulated into the multispectral bandwidths of the WorldView-3 satellite and the Micasense RedEdge-MX unoccupied aerial vehicle sensors and vegetation indices were calculated to compare detection limits of kelp with a focus on differences between red edge and near infrared indices. For kelp on the surface, near-infrared reflectance was higher than red-edge reflectance. Once submerged, the kelp spectra showed two narrow reflectance peaks in the red-edge and near-infrared wavelength ranges, and the red-edge peak was consistently higher than the near-infrared peak. As a result, kelp was detected deeper with vegetation indices calculated with a red-edge band versus those calculated with a near infrared band. Our results show that using red-edge bands increased detection of submerged kelp canopy, which may be beneficial for estimating kelp surface-canopy area and biomass.

2.2 Introduction

Kelp forests are highly productive three-dimensional coastal marine habitats (Druehl & Wheeler, 1986; Kain, 1987) that provide a number of environmental services and contribute substantial economic value to coastal communities globally (Krumhansl *et al.*, 2016). In the northeast Pacific, the two dominant surface-canopy forming kelp species, *Nereocystis luetkeana* and *Macrocystis pyrifera* (Druehl, 1970), stabilize shorelines via wave dampening (Jackson, 1984; Mork, 1996), support economically important fisheries (Krumhansl & Scheibling, 2012; Olson *et al.*, 2019), and are commercially harvested for various purposes (Stekoll *et al.*, 2006; Springer *et al.*, 2007). However, both kelp species are subject to high spatial and temporal variability, correlated with biotic and abiotic drivers of change (Pfister *et al.*, 2017; Bell *et al.*, 2020). As such, resource managers are incentivized to monitor the status of these kelp forests, and the corollary effects of the ecosystem services they provide (Stekoll *et al.*, 2006; Pfister *et al.*, 2017; Cavanaugh *et al.*, 2021a), a task that has been facilitated by remote sensing since the mid-20th century (Jensen, 1980; Pfister *et al.*, 2017).

Generally, the remote sensing of surface-canopy forming kelp forests aims to detect the portion of the kelp that forms a canopy, floating at the water's surface; using sensors aboard Earth Observation Satellites (EOS) (Cavanaugh *et al.*, 2010; Schroeder *et al.*, 2019b), piloted aircraft (Stekoll *et al.*, 2006; Pfister *et al.*, 2017), and Uncrewed Aerial Vehicles (UAVs) (Cavanaugh *et al.*, 2021b). In order to use the data provided by remote sensing platforms effectively, it is crucial to understand factors that influence the spectral signature of kelp canopy in water (Schroeder *et al.*, 2019b). Floating kelp canopy has high reflectance in the near-infrared wavelength range (NIR) (700–1000 nm), which contrasts with the high NIR absorption by the surrounding water, allowing for binary classification of floating kelp canopy and water within an image (Jensen,

1980). However, there are numerous considerations (e.g., sun glint, bathymetry, turbidity; see (Schroeder *et al.*, 2019b; Cavanaugh *et al.*, 2021a)) that can reduce the separability between the spectral values of kelp canopy and water. One crucial factor that can affect the ability to detect kelp canopy is the submersion of the canopy by tides and associated tidal currents, which can dampen the NIR reflectance of kelp and lead to potential errors when estimating kelp area or biomass (Schroeder *et al.*, 2019a; Cavanaugh *et al.*, 2021b).

In an attempt to minimize classification errors associated with kelp submergence, remote sensing imagery is often acquired at low tides during the peak growing season (mid-late summer) when the majority of the kelp canopy is floating at the water's surface (Stekoll *et al.*, 2006; Schroeder *et al.*, 2019a; Hamilton *et al.*, 2020). However, there are multiple reasons why a remote sensor may also want to detect the submerged portion of the kelp canopy. For example, the northeast Pacific coastline often experiences non-ideal weather conditions for remote sensing data acquisition, leading to imagery being opportunistically collected at higher than ideal tidal heights when more kelp canopy is more likely to be submerged compared to ideal low tide conditions (Schroeder *et al.*, 2019b; Cavanaugh *et al.*, 2021a). Further, the fixed rate of EOS orbits may result in some regions only having imagery available during high tides even if acquisition conditions are otherwise ideal (Cavanaugh *et al.*, 2021a). Even if remote sensing imagery is captured during ideal tide and weather conditions, portions of kelp canopy may also be continuously submerged depending on the species being targeted. Specifically, if a remote sensor is targeting detection of *Nereocystis luetkeana* (hereafter, *Nereocystis*) surface canopy, one has to consider the two distinct structures with varying buoyancy, the bulb and blades. The bulb is a roughly cylindrical gas-filled structure that floats on the surface of the water and is anchored to the sea floor by a stipe and holdfast (Springer *et al.*, 2007). The blades are long thin structures

that trail from the end of the bulb, often with many individuals around four meters long per bulb (Springer *et al.*, 2007). The blades are not buoyant and are likely to remain submerged below the water's surface regardless of tidal height (Britton-Simmons *et al.*, 2008; Schroeder *et al.*, 2019b). In addition, floating portions of kelp canopy may be periodically submerged in areas with especially strong currents (Britton-Simmons *et al.*, 2008). Therefore, it is important to understand how submersion of kelp canopy affects the reflectance in the NIR range, as well as whether certain spectral features may allow for higher detectability of kelp when collecting remote sensing imagery from different platforms.

In the past, the red-edge (RE) spectral region (670–750 nm), which includes a range of the shortest NIR wavelengths, has traditionally been used to determine health characteristics of terrestrial plants (Filella & Penuelas, 1994). However, these wavelength ranges also penetrate deeper into the water column than longer NIR wavelength ranges (Pegau *et al.*, 1997), resulting in the potential for higher above water reflectance in the RE than the longer NIR for submerged vegetation (Han & Rundquist, 2003; Kearney *et al.*, 2009; Turpie, 2013; Song & Park, 2020). Therefore, given the spectral similarities between kelps and other types of vegetation, it is reasonable to assume that the RE wavelength range may also be beneficial for detecting submerged kelp canopy. Hereafter, the term NIR will refer to only the longer wavelength range above 751 nm, to avoid confusion with the NIR wavelength range that overlaps the RE wavelength range.

To date, there have been no direct comparisons of the ability to detect submerged kelp when using RE or NIR wavelength ranges. Additionally, while the submersion kelp canopy due to tides and currents is well documented using various sensors with different spatial and spectral resolutions (Britton-Simmons *et al.*, 2008; Nijland *et al.*, 2019; Schroeder *et al.*, 2019a;

Hamilton *et al.*, 2020; Bell *et al.*, 2020; Cavanaugh *et al.*, 2021b), there has been no characterization of the changes to the above water spectra of kelp as the canopy is submerged, nor any investigation of the band combinations used in vegetation indices in relationship to accurate detection of the submerged kelp canopy. With this is mind, our goal was to characterize changes to above-water reflectance of different *Nereocystis* canopy structures as they were submerged and to relate those changes to depth detection limits. To accomplish this goal, we performed (1) an experiment that documents the effects of kelp submersion on the above-water hyperspectral reflectance of both *Nereocystis* bulb and blade structures. We also compared (2) the detection limits of submerged kelp using RE and NIR vegetation indices, which were calculated from the simulated multispectral bands of high spatial-resolution air- and space-borne sensors.

2.3. Methods

2.3.1 Spectral Data Acquisition and Processing

The kelp submergence experiment took place on a marina dock in Victoria BC, on a sunny, cloudless day in September 2020. The Secchi depth during the time of the experiment was 7.5 m, showing relatively clear water, similar to general conditions for the coastal waters of the Salish Sea at the same time of year with low influence from riverine discharge, and low levels of total suspended-matter, chlorophyll-a, and colored dissolved organic matter present in the water column (Phillips & Costa, 2017). While the ranges of both Nereocystis and Macrocystis overlap on the British Columbia coast, only Nereocystis is found around the southern tip of Vancouver Island where this study occurred. The location and timing of the experiment allowed for the control of four criteria that we required: (1) controlled sea-state; with the dock acting as a shelter from any slight breezes, thereby minimizing variability in glint or light refraction due to ripples

or waves on the water (Mobley, 1994); (2) platform stability, which minimized the potential errors during spectral acquisition due to the movement of both kelp and sensor that might occur in situ from a boat; (3) maintained environmental conditions expected in situ during peak biomass for local kelp, such as the inherent optical properties of water and optical constituents within the water column that would be difficult to reproduce in vitro; (4) a water depth (12 m) greater than the Secchi depth to minimize the influence of substrate reflectance on the above-water reflectance signal (Dierssen *et al.*, 2015; Hu *et al.*, 2017).

The experiment consisted of four separate trials. For each trial, a sample of *Nereocystis* was attached to a black frame made of high-density polyethylene (a plastic with low reflectance across the visual and near-infrared wavelength ranges), which was submerged from the surface to 100 cm in 10 cm increments on the sunlit side of the dock (Figure 1). Before each trial, radiance measurement of a Spectralon white-reference panel ($L_{spec(\lambda)}$) and an internal dark-current reading were taken to calculate reflectance (Table 1; Equation (1)) and reduce noise in the spectral data (ASD, 2017). During each trial, ten individual above-water hyperspectral radiance measurements ($L_{T(\lambda)}$) of kelp were collected at each incremental depth. Two of the four trials used the *Nereocystis* bulb, and two trials used the *Nereocystis* blades. Therefore, in total, 20 measurements of $L_{T(\lambda)}$ were collected for each kelp structure (bulb or blades) at each depth. After each trial, 10 radiance measurements were taken of the sky ($L_{sky(\lambda)}$) to be used in sky glint corrections (Mobley, 1999). Additionally, a total of 60 $L_{T(\lambda)}$ measurements were taken of water with no kelp within the field of view as a baseline for comparison with submerged kelp.

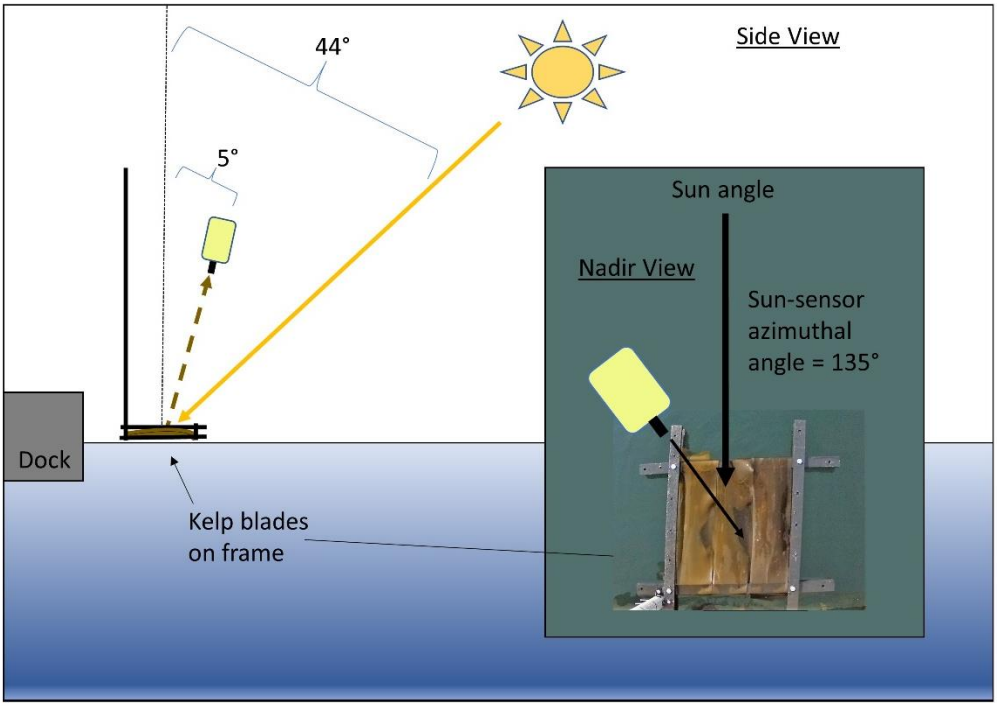

Figure 1. Side view of submergence experiment showing the geometry of acquisition for spectroradiometer and angle of zenith for the sun. Inset shows nadir view of the experiment with the azimuthal angle between spectroradiometer and sun and kelp blades inside the black frame. Diagrams are not to scale.

Table 1. Spectral parameters used to calculate above-water reflectance, as per Equation (1). All spectral measurements were collected using a calibrated ASD Fieldspec Handheld2 spectroradiometer with a one-degree fore optic (full viewing-angle), which detects a wavelength range from 325–1075 nm at 1 nm increments.

Symbol	Name	Units	Angle from Nadir	Sun-Sensor Azimuthal Angle
λ	Wavelength	nm	-	-
L_T	Above-water radiance	$\mu W\ cm^{-2}sr^{-1}nm^{-1}$	5°	135°
L_{spec}	White panel radiance	$\mu W\ cm^{-2}sr^{-1}nm^{-1}$	5°	135°
L_{sky}	Sky radiance	$\mu W\ cm^{-2}sr^{-1}nm^{-1}$	175°	135°
ρ'	Proportionality factor	-	-	-

The solar elevation angle during the experiment was 46°, which ensured sun-glint did not contaminate the spectra based on our geometry of acquisition (Mobley, 1999; Mount, 2005). $L_{T(\lambda)}$ measurements were taken at 5° from a nadir viewing angle to avoid reflection of the white spectroradiometer in the field of view on the water surface, and a sensor-sun azimuthal angle of

135° was used to minimize specular reflection in the field of view (FOV) (Mobley, 1999). $L_{sky(\lambda)}$ measurements were taken at 5° from zenith at the same azimuthal angle as $L_{T(\lambda)}$. The spectroradiometer was held one meter above water, giving a footprint ranging from about 1.6 cm at the surface to 3.8 cm when the target was 100 cm deep. This small footprint was meant to ensure that the $L_{T(\lambda)}$ measurements contained 100% kelp, avoiding mixed pixel considerations (Cavanaugh *et al.*, 2011).

$$R(\lambda)_{0+}(\%) = \left(\frac{\left(L_T(\lambda)\right)}{\left(L_{spec}(\lambda)\right)} - \frac{\left(\rho' \cdot L_{sky}(\lambda)\right)}{(L_{spec}(\lambda))} \right) \times 100 \qquad (1)$$

Here, ρ' was the proportionality factor of 0.0211, which relates the radiance measured directly from the sky to the estimated amount of sky radiance reflected off the sea surface based on wind, cloud cover, and geometry of acquisition (Mobley, 1999). $R(\lambda)_{0+}(\%)$ for kelp at the surface (0 cm) was not subjected to the sky glint correction. Hereafter, $R(\lambda)_{0+}(\%)$ values for kelp on the surface, submerged kelp, and water with no kelp are referred to as R_{0+} for brevity.

The R_{0+} spectra were first smoothed using a mean filter with a window of 5 nm to reduce noise while maintaining spectral features, and all spectra were then manually inspected for quality control. All bulb spectra were highly consistent, however, some blade spectra showed deviations in both the blue-green and NIR regions; likely due to water movement between blades as kelp was submerged, causing opened gaps in the "canopy" of blades attached to the platform. These spectra likely did not contain 100% blades within the field of view and were therefore removed from further analysis (Table 2). Despite the removal of some blade spectra, the smallest sample size at any depth after quality control was at 90 cm with n = 10 spectral samples. Therefore, we do not expect that these removals biased the results of this study.

Table 2. Total number of each class of spectra before and after quality control was performed.

Spectral Sample Type	Samples Collected	Samples Removed during Quality Control	Samples Used in Analysis
Bulbs (surface-100 cm)	220	0	220
Blades (surface-100 cm)	220	51	169
Water	60	0	60
Sky	40	0	40

2.3.2 Simulation of Micasense and WorldView Band R_{0+} and Indices

After sky-glint correction, smoothing, and quality control of the spectra, R_{0+} measurements were simulated into bands of the WorldView-3 (R_{0+WV3}) and the Micasense RedEdge-MX (R_{0+MSRE}) sensors (Micasense, 2019; Maxar, 2020). These sensors were chosen because both have a relatively high spatial resolution (WV3: 1.84 m; MSRE: ~1–10 cm), which is ideal for mapping kelp canopy in nearshore regions where it is likely to be submerged by tides and currents (Schroeder *et al.*, 2019b). The R_{0+} at the bands of these sensors were simulated using Gaussian functions to estimate the sensor's spectral response for each band, based on full-width half maximum values of each sensor's band (Figure 2; Table 3). For a direct comparison, only the VNIR bands shared by both sensors were used for simulations.

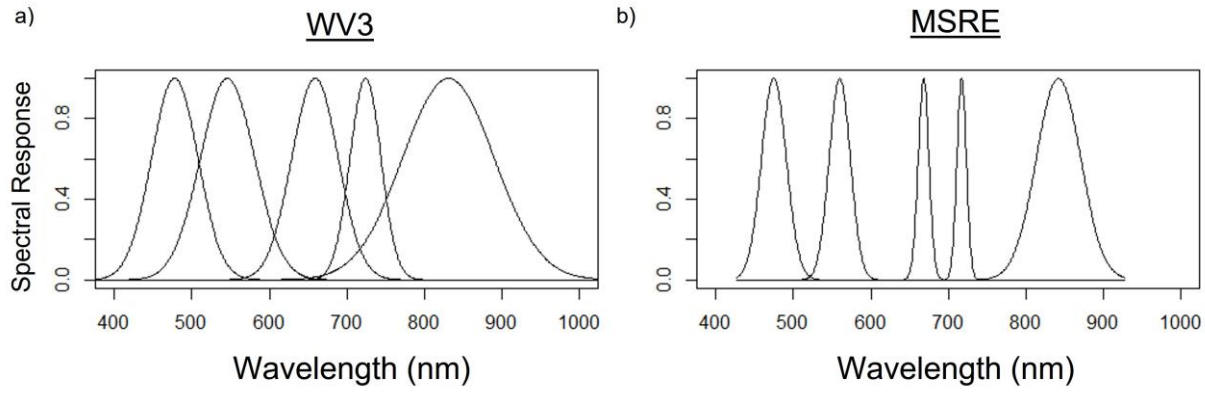

Figure 2. Relative spectral responses at each band according to Gaussian functions were used to simulate the shared bands of (**a**) WorldView-3 (WV-3) earth observation satellite and (**b**) Micasense RedEdge-MX (MSRE) uncrewed aerial vehicle sensors—from left to right: blue, green, red, red-edge, and near-infrared band locations are shown.

Table 3. The effective bandwidths of the overlapping bands for both WorldView-3 (WV3) and Micasense RedEdge-MX (MSRE) sensors.

Band	WV3	MSRE
Blue	445–517 nm	459–491 nm
Green	507–586 nm	546.5–573.5 nm
Red	626–696 nm	661–675 nm
Red-edge	698–749 nm	711–723 nm
Near-infrared	765–899 nm	813.5–870.5 nm

2.3. Normalized Vegetation Indices

Once the hyperspectral data were simulated into the respective sensor bands, the R_{0+} at these bands were used to calculate normalized vegetation indices (VI_n; Equation (2)), which are commonly used to enhance spectral features of interest and reduce sensitivity to environmental influences within remote sensing imagery (Rouse *et al.*, 1974; Tucker, 1979). We tested several band combinations for VI_n as different band combinations may increase or decrease the separability between kelp and water in an image (Augenstein *et al.*, 1991).

$$VI_n = \frac{\text{band 2} - \text{band 1}}{\text{band 2} + \text{band 1}} \quad (2)$$

Because naming conventions for different VI_n combinations are not ubiquitous across published literature, here, we referred to each VI_n as the order in which bands appeared in the numerator of the VI_n equation, separated by an underscore (Table 4).

Table 4. Vegetation indices calculated from simulated multispectral data.

Vegetation Index (VI_n)	VI_n Equation
RE_R	$\frac{RE - red}{RE + red}$
RE_G	$\frac{RE - green}{RE + green}$
RE_B	$\frac{RE - blue}{RE + blue}$
NIR_R	$\frac{NIR - red}{NIR + red}$
NIR_G	$\frac{NIR - green}{NIR + green}$
NIR_B	$\frac{NIR - blue}{NIR + blue}$

One of the most commonly used VI_n for kelp mapping is NIR_R, which was originally used to detect terrestrial vegetation because of the high NIR and low red signal (Rouse *et al.*, 1974), but has since been used for kelp canopy detection due to the similar spectral characteristics between kelp canopy and terrestrial vegetation (Jensen, 1980). More recently, NIR_R has been positively correlated with both the areal extent and biomass of kelp canopy (Cavanaugh *et al.*, 2010; Schroeder *et al.*, 2019a; Hamilton *et al.*, 2020). However, various other combinations of visible and NIR bands have been used for kelp canopy detection with multispectral sensors. For instance, Schroeder et al. (2019b) used NIR_R and NIR_G for kelp detection with the WorldView-2 imagery. The NIR_G combination may be more accurate for detecting a wide range of chlorophyll levels (Gitelson *et al.*, 1996) and has generally been found comparable with NIR_R in the detection of both floating and submerged vegetation (Song & Park, 2020). Stekoll

et al. (2006) found that NIR_B and NIR_G both provided higher kelp canopy and water separability in aerial imagery than NIR_R. Further, recent comparisons with multispectral UAV and satellite imagery have shown that RE indices can improve separability of Macrocystis canopy and water when compared with NIR based indices (Mora-Soto *et al.*, 2020; Cavanaugh *et al.*, 2021b), although this improvement was not specifically attributed to improved detection of submerged portions of the kelp canopy in either study.

Here, we compared the statistical differences in NIR and RE-based VI_n values. R_{0+MSRE} and R_{0+WV3} bands were used to calculate NIR_B, NIR_G, NIR_R, and RE_B, RE_G, and RE_R for both bulb and blades separately, for each depth. The statistical analysis was comprised of (i) VI_n values compared with one another at each depth from the surface to 100 cm, and (ii) VI_n values for water (with no kelp) compared to one another. First, the dataset was tested for normality, and while quantile–quantile plots suggested reasonable normality of the data distributions, Levene's test showed nearly all groupings for comparison displayed heterogeneity in variance. Therefore a non-parametric test was used in the analysis (Schultz, 1985). The Welch's ANOVA test was used to determine whether significant differences between VI_n existed at each depth, and the Games–Howell post hoc test was used to determine which indices were significantly different from one another (Algina *et al.*, 1994; Shingala & Rajyaguru, 2015). As part of the analysis, we focused on the statistical results comparing the RE and NIR counterpart indices only (e.g., NIR_R & RE_R, or NIR_B & RE_B) at each depth.

2.3.4 Threshold Selection and Depth Limits for Kelp Detection

Once a VI_n has been selected for classifying kelp in remote sensing imagery, a VI_n value is then chosen as a threshold to classify the kelp and water within the imagery. For example, Cavanaugh et al. (2010) selected a threshold based on the 99.98th percentile highest NIR_R value from a

histogram of known ‘deep water’ pixels, and Nijland et al. (2019) determined a NIR_R value of 0.05 to be a reasonable threshold by comparing pixel values of sparse kelp and open water. Since the R_{0+} values of water vary spatially and temporally according to optical constituents and inherent optical properties of water, as well as the characteristics of local substrate and bathymetry (Morel & Prieur, 1977; Phillips & Costa, 2017; Vahtmäe *et al.*, 2020), these thresholds are often ‘dynamic’, and are therefore determined on an image-by-image basis. For satellite or airborne imagery covering a large regional scale, it may even be appropriate to select multiple thresholds across different regions within an image.

We determined a dynamic threshold for each VI_n based on the maximum VI_n value measured for water during the experiment following Cavanaugh et al. (2010). The depth where the mean VI_n value of submerged kelp dropped below the dynamic threshold value was considered the depth where kelp was spectrally indistinguishable from water. Since our experiment was conducted under ideal conditions (flat calm water, full sun, etc..) the dynamic thresholds were all negative values and the maximum depth of detection using these thresholds likely overstate the potential depths for kelp detection in actual remote sensing imagery. Therefore, we also used a second VI_n threshold of zero, based on the theoretical spectral properties of kelp within an individual pixel that contains 100% kelp. For example, within a pixel, if the R_{0+} value of band 2 (RE or NIR) equals the R_{0+} value as band 1 (the visible band), the numerator in the VI_n equation (Equation 2), and therefore the overall VI_n value for that pixel, equals zero. This conservative threshold is closer to the values of 0.05 and 0.003 determined from remote sensing imagery by Nijland et al. (2019) and Mora-Soto et al. (2020), respectively.

Depth detection limits were reported to the nearest 10 cm depth on the shallow side of the threshold because the kelp was submerged in 10 cm intervals. To determine whether the

detectable kelp (values above the threshold) and non-detectable kelp (values below the threshold) were statistically separable, the means for kelp measurements immediately above and below the threshold were compared for significant differences using Welch's t-test (Welch, 1947).

2.4 Results

Here, we present the spectral characteristics of *Nereocystis* bulbs and blades as they are each submerged from the surface to 100 cm, as well as the changes seen in the hyperspectral data when they are simulated into multispectral sensor bandwidths. Next, we show VI_n comparisons for kelp, focusing on comparing the RE and NIR counterpart indices (e.g., NIR_R & RE_R, or NIR_B & RE_B) at each depth, and finally, we present the depth detection limits for each VI_n as determined by both dynamic and conservative thresholds.

2.4.1 Spectral Characteristics of Surface and Submerged Kelp

Overall, Overall, the R_{0+} of both *Nereocystis* bulbs and blades showed similar placement of spectral features, however, the magnitude of reflectance at these features was different (Figure 3a,b). For *Nereocystis*, spectral features in the visible wavelength ranges are largely due to absorption by a combination of chlorophyll-a, chlorophyll-c, and fucoxanthin pigments, which are characteristic pigments of bull kelp, as well as other kelp species (Wheeler *et al.*, 1984; Olmedo-Masat *et al.*, 2020). Accordingly, here we saw a broad absorption feature in the 400–550 nm range and narrower absorption features around 633 and 675 nm for both bulbs and blades at the surface. These absorption features resulted in reflectance peaks at 575, 600, and 645 nm for both bulbs and blades (Figure 3a,b, insets). In the NIR region, broad reflectance peaks were detected from 690 nm (RE) to 900 nm (NIR) (Figure 3a,b, insets) and small, narrow peaks centered at 761 nm were observed (Figure 4a,b).

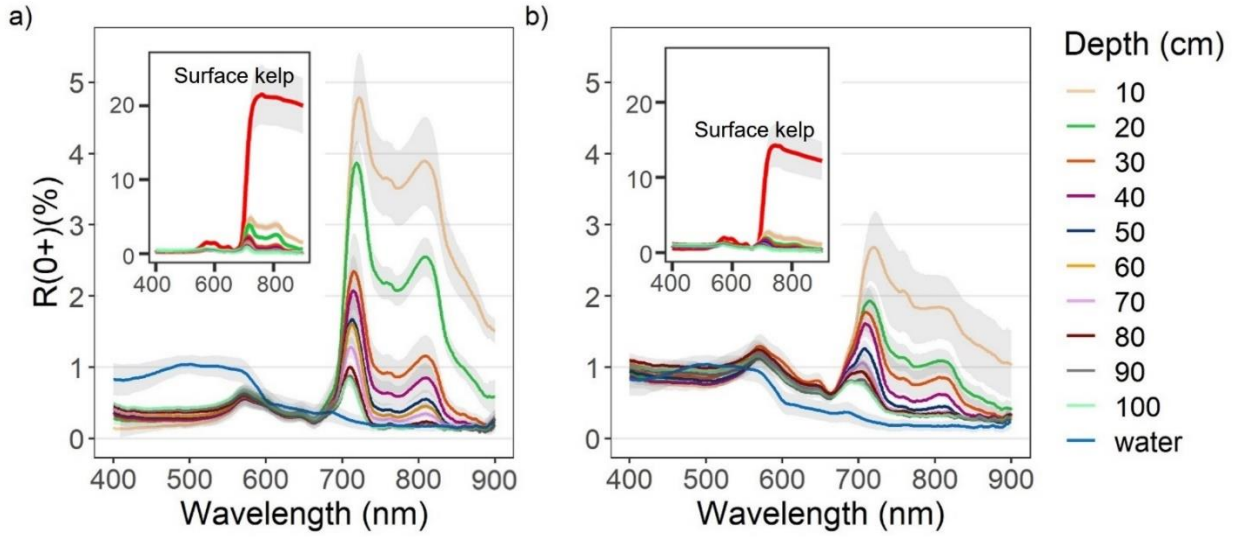

Figure 3. Reflectance values (R_{0+}) between 400–900 nm (mean +/− sd) of water with (**a**) Nereocystis bulbs, and (**b**) Nereocystis blades, at incremental depths below water surface. The inset plots contain spectra of bulbs and blades on the surface compared to the same spectra of submerged bulb and blades as in the main plots, for the purpose of showing the difference in magnitude.

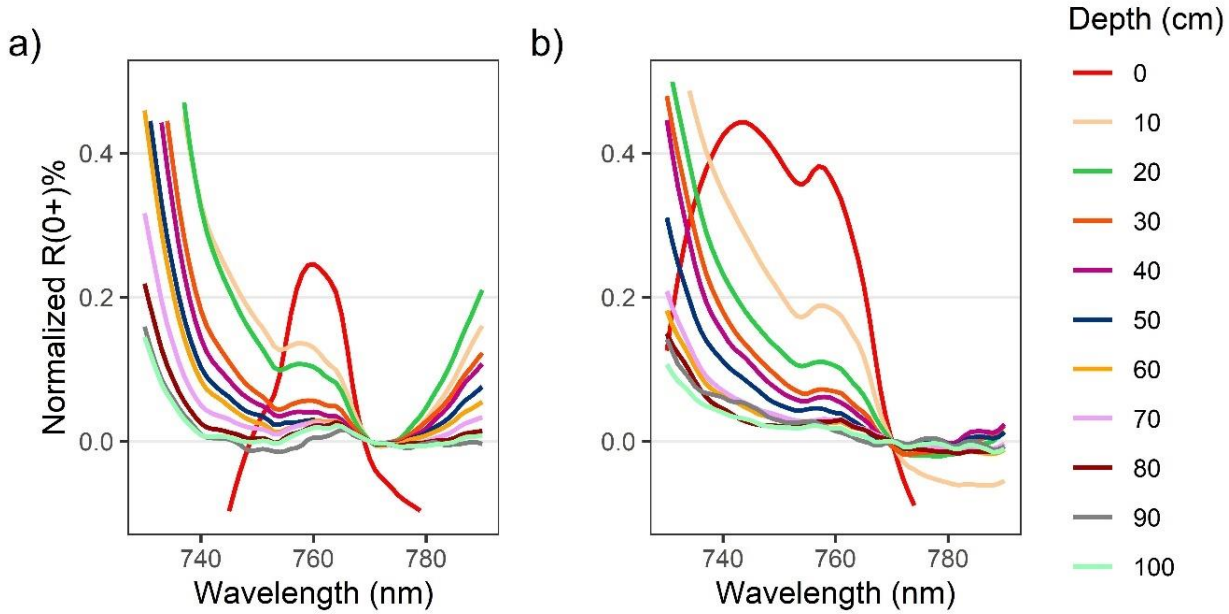

Figure 4. Zoomed in plot showing solar-induced chlorophyll fluorescence (SICF) peaks centered at 761 nm for above-water R_{0+} for Nereocystis bulbs (**a**) and blades (**b**) at incremental depths below the water surface. Spectra are normalized at 770 nm to show relative changes to the shape of the SICF peak with submergence.

When kelp structures were submerged, the influence of the water and its constituents on the R_{0+} signal increased with submersion for both bulb and blades. The decreases in R_{0+} in the RE and NIR region were far greater than decreases in R_{0+} observed across the visible region of the spectra (Figure 3a,b, insets). With initial submersion below the water's surface, the largest declines in the visible wavelength ranges were seen at 600 nm and 645 nm, although all peaks in the visible region continued to decrease with submersion (Figure 3a,b). While the R_{0+} at the absorption feature between 400–550 nm initially decreased with submersion, the reflectance then rose as the depth of submersion increased. In the NIR region of spectra for both structures, once kelp was submerged, the broad NIR peaks were replaced by two peaks centered around 715 nm and 815 nm (Figure 3a,b), hereafter referred to as the RE peak and the NIR peak, respectively. At each depth, the R_{0+} at the RE peak was higher than the NIR peak. As submergence increased, the position of the RE peak shifted toward lower wavelengths within the RE wavelength ranges while the position of the NIR peaks remained relatively stable. The small peaks at 761 nm remained stable, but decreased in magnitude with submersion, becoming difficult to visibly distinguish around 50 cm depth (Figure 4a,b).

R_{0+WV} and R_{0+MSRE} showed the same general patterns as the hyperspectral data (Figure 5a,b,c,d). However, some spectral information was lost with the reduction of spectral resolution, such as the location and magnitude of different peaks. Overall, the differences in width and placement of bands resulted in only small differences in R_{0+WV3} and R_{0+MSRE} band values (Figure 5). For both bulbs and blades at the surface, differences in the visible wavelength ranges between R_{0+WV} and R_{0+MSRE} were less than 0.8% for the red, blue, and green bands, and these differences became even smaller as kelp was submerged. In the RE and NIR bands, differences between R_{0+WV} and R_{0+MSRE} were less than 0.3% on the surface. Once submerged to 10 cm, differences between

R_{0+WV} and R_{0+MSRE} increased to 1.8% in the NIR bands and 0.5% in the RE bands, although similar to the visible bands, the differences between R_{0+WV} and R_{0+MSRE} also became smaller as the kelp was submerged deeper.

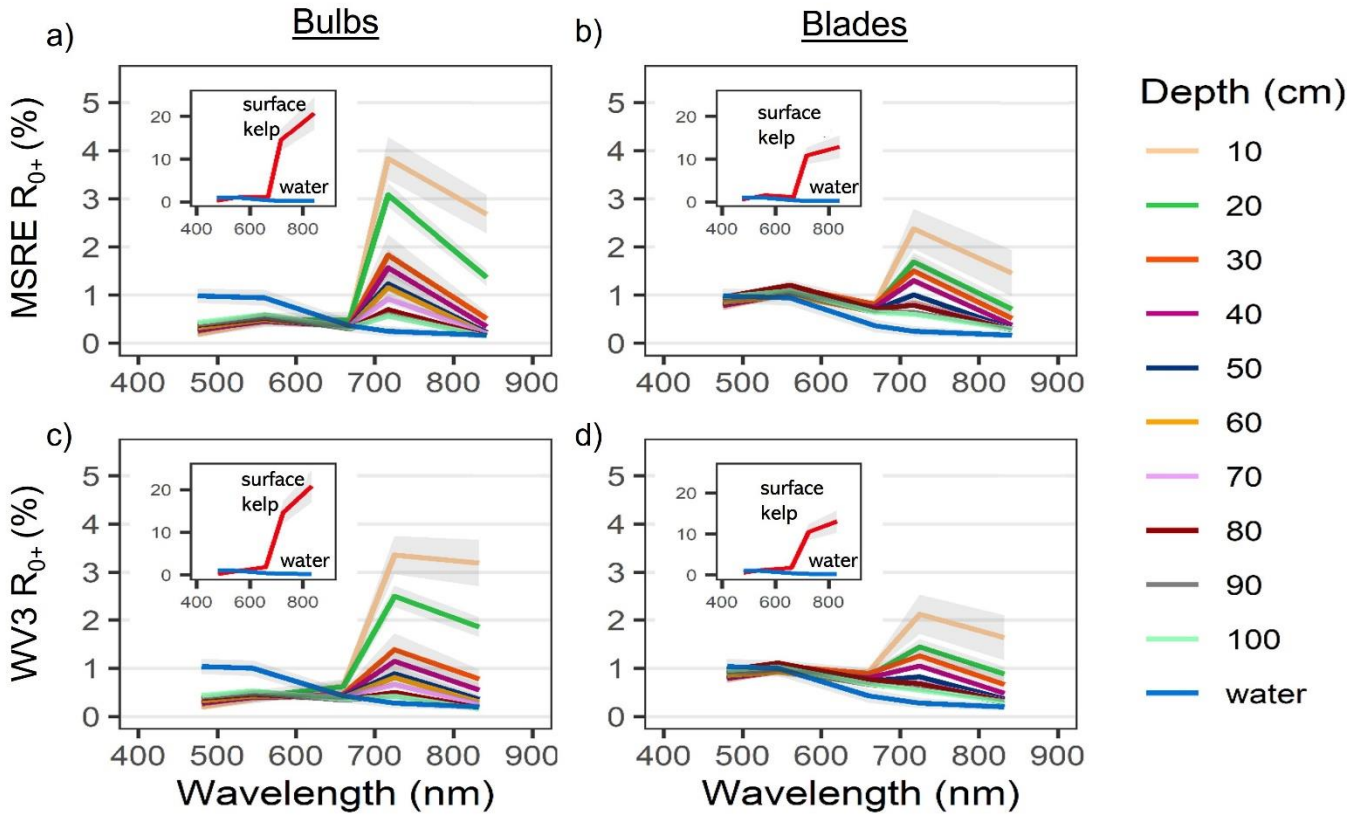

Figure 5. Reflectance values (R0+) for bulbs (**a,c**) and blades (**b,d**) of simulated bands (mean +/− sd) shared by the Micasense RedEdge-MX (MSRE; **a,b**) and WorldView-3 (WV3; **c,d**), derived from the hyperspectral data (Figure 3) using Gaussian response functions (Figure 2).

2.4.2 Vegetation Indices: Signal Strength and Depth-detection Limits of Submerged Kelp

Generally, RE VI_n values were higher than NIR VI_n values at a given depth as kelp was submerged (Figure 6). For bulbs, RE VI_n values decreased linearly from the surface to 100 cm, while NIR VI_n showed a steeper linear decrease over the first 50 cm, followed by an inflection point and a lesser decline towards 100 cm. For blades, trendlines of both NIR and RE VI_n resemble exponential functions, with the NIR VI_n displaying a steeper decrease of values than the RE VI_n.

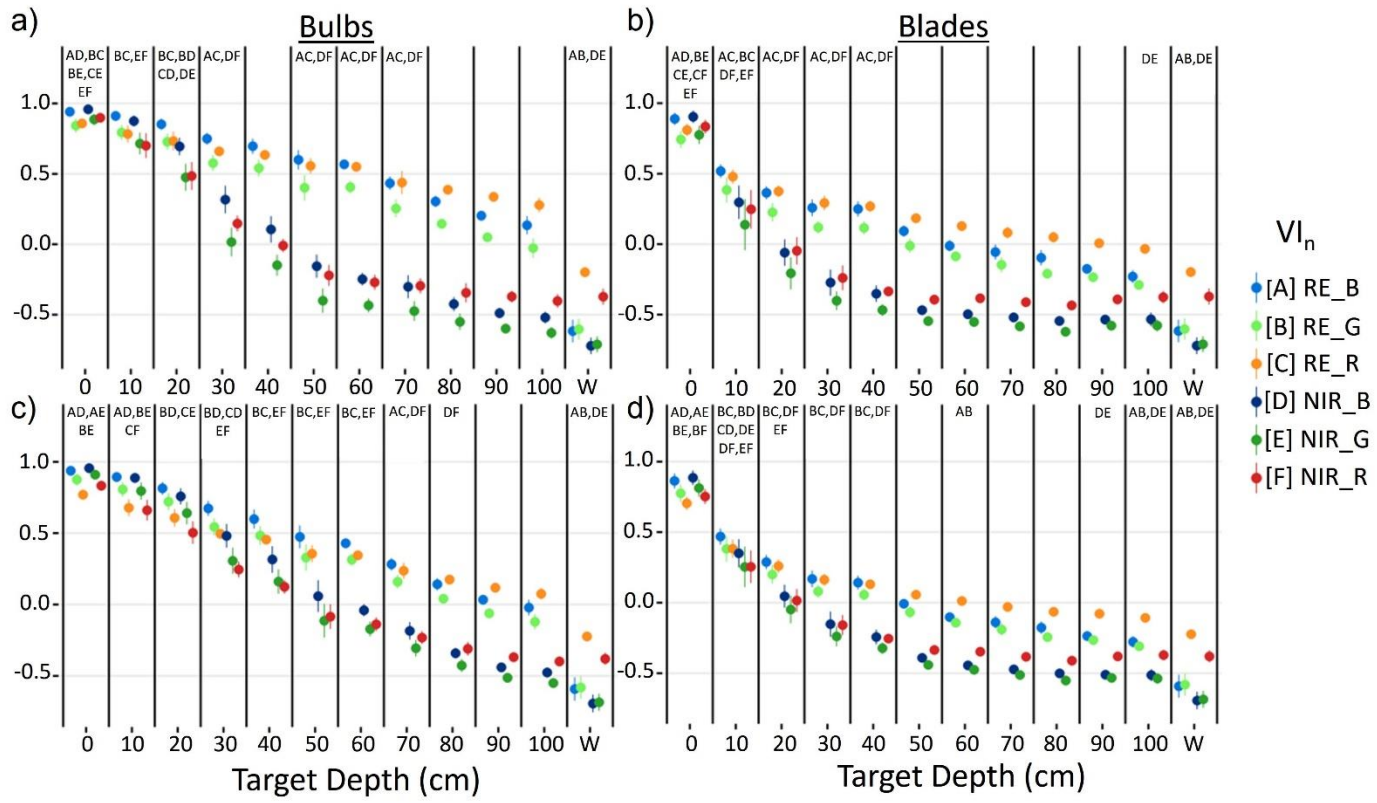

Figure 6. Mean +/− sd of vegetation index (VI_n) values for Nereocystis bulbs (**a,c**) and blades (**b,d**), submerged from the surface to 100 cm and water; derived from simulated Micasense RedEdge-MX (MSRE; **a,b**) and WorldView-3 (WV3; **c,d**) bandwidths. Paired letters above each column represent no significant differences ($p \geq 0.05$) between mean index values at that depth.

Specifically, the Games–Howell post hoc tests showed that for kelp at the surface, RE VI_n values were either smaller than or not significantly different from their counterpart NIR indices (Figure 6), depending on the visible band used. Once kelp was submerged, RE VI_n values were significantly greater than their NIR counterparts at each depth with the MSRE sensor. However, with the WV3 sensor, RE VI_n values were not significantly greater than their NIR counterparts until 10 cm and 20 cm depth for blades and bulbs, respectively. All VI_n values for water were negative, meaning that the R_{0+} at the visible band used in the VI_n was higher than the R_{0+} at the RE or NIR band used in the VI_n, regardless of sensor simulation or index combination. RE_R consistently showed the highest values for water, followed by NIR_R, and there were no

significant differences between RE_B and RE_G water values, nor for NIR_B and NIR_G water values. Here, we focused on the statistical results comparing the RE and NIR counterpart indices only (e.g., NIR_R & RE_R, or NIR_B & RE_B) at each depth, however, Figure 6 displays paired letters to indicate all pairs of VIn where no significant difference between VIn pairs was detected.

The depth detection limits varied based on sensor type, kelp structure, and thresholding method (Table 5; Figure 7). Overall, when using the conservative (more realistic) threshold of zero, RE VI_n showed detection of kelp at least twice as deep as NIR VI_n, and bulbs were detectable at greater depths than blades. Detection limits for the same VI_n between sensors were generally within a range of 0–20 cm apart, although in a few cases (e.g., RE_R) these differences were larger. In addition, the choice of different visible bands for a VI_n only resulted in detection limit differences up to 20 cm, with RE_R once again proving the exception. No RE indices crossed below the dynamic thresholds at 100 cm depth, meaning RE indices could detect kelp to at least 100 cm depth with these thresholds, while NIR indices could generally detect kelp to around 100 cm depth or less. In all cases, the RE indices at 100 cm depth were more separable from water than the NIR indices at the same depth. The use of different visible bands in the VI_n combination generally resulted in detection limit differences of 0–30 cm for bulbs. For all measured depth detection limits, the index values measured at the increments 10 cm above and below the threshold remained divergent ($p < 0.05$), suggesting that all the measured results for conservative and dynamic thresholds are accurate to at least 10 cm increments.

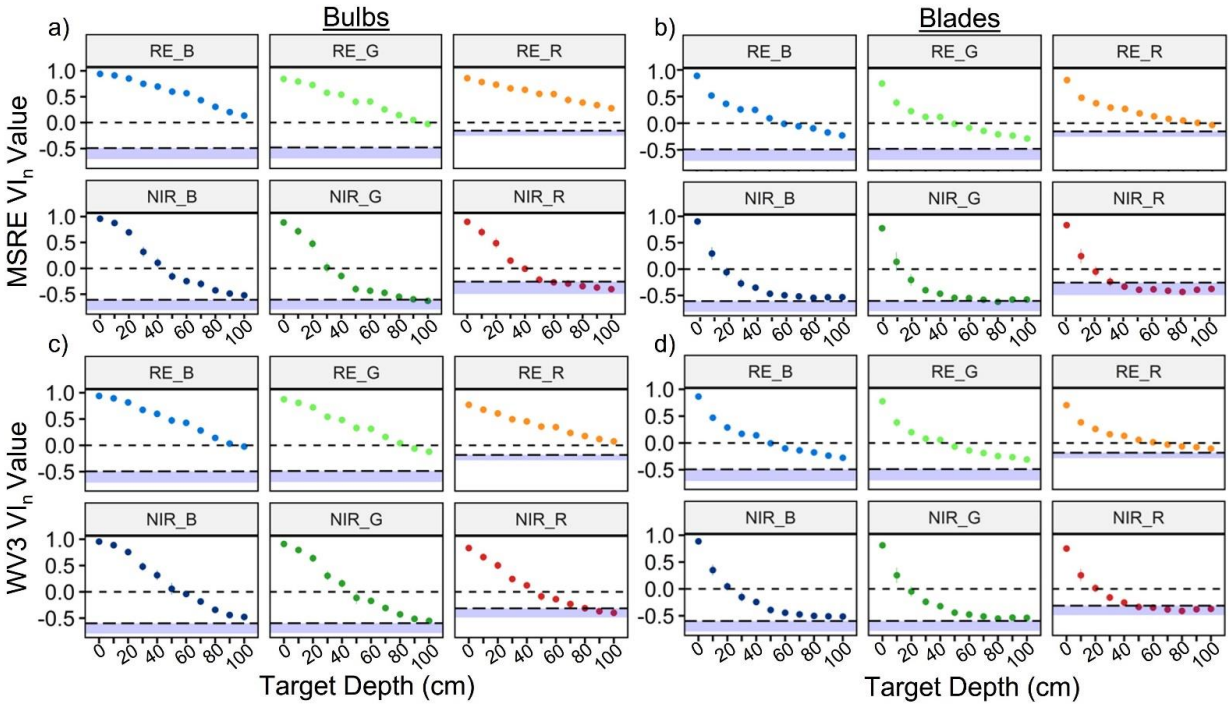

Figure 7. Mean +/− sd of vegetation index (VI_n) values for Nereocystis bulbs (**a,c**) and blades (**b,d**) submerged from the surface to 100 cm. derived from simulated Micasense RedEdge-MX (MSRE; **a,b**) and WorldView-3 (WV3; **c,d**) bandwidths. The black dashed lines at 0 represent the more conservative and realistic threshold, and the blue bars represent the full range of water values for each respective index, with the adjacent dashed lines representing the dynamic threshold.

Table 5. Depth detection limits (cm) based on conservative threshold of 0.0 and the dynamic thresholds (maximum water value) for Nereocystis bulbs and blades, as simulated to Micasense RedEdge-MX (MSRE) and WorldView-3 (WV3) bandwidths.

Index			**RE_B**	**RE_G**	**RE_R**	**NIR_B**	**NIR_G**	**NIR_R**
MSRE	**Bulb**	**Conservative (0.0)**	>100	90	>100	40	30	30
		Dynamic (max.)	>100	>100	>100	>100	90	50
	Blade	**Conservative (0.0)**	50	40	90	10	10	10
		Dynamic (max.)	>100	>100	>100	>100	>100	30
WV3	**Bulb**	**Conservative (0.0)**	90	80	100	50	40	40
		Dynamic (max.)	>100	>100	>100	>100	>100	80
	Blade	**Conservative (0.0)**	40	40	60	20	10	20
		Dynamic (max.)	>100	>100	>100	>100	>100	40

2.5 Discussion

Overall, we found that submersion of kelp in water changes the shape and magnitude of R_{0+} in the RE and NIR region of kelp spectra (Figure 3), and *Nereocystis* bulbs had a higher magnitude R_{0+} in the RE and NIR region than blades (Figure 3). We also observed that RE VI_n values for submerged kelp had higher separability from water than their NIR counterparts (Figure 6), meaning that kelp can be positively classified at deeper depths when using an RE VI_n (Table 3; Figure 7). Our results also showed that VI_n that used a visible band with high R_{0+} (e.g., green or blue) had worse detectability for submerged kelp than a VI_n that used a visible band with low R_{0+} (e.g., red). Together, these findings have important implications for the application of kelp remote sensing to the applied monitoring of kelp forests.

2.5.1 Spectral Characteristics of Kelp as it is Submerged

A broad R_{0+} peak across the NIR region was observed for surface measurements of *Nereocystis* as a result of the interaction of light with the cellular structure of the kelp (Liew *et al.*, 2008). Once submerged, our experiment showed two key changes in the NIR region of the kelp spectra (Figure 3), both due to characteristic absorption features of water: (1) the splitting of the single broad NIR peak into two narrower RE and NIR peaks due to prominent water absorption feature at 760 nm (Ruru *et al.*, 2012) and (2) higher R_{0+} at the RE peak versus the NIR peak, resulting from the continually increasing absorption of light by water above 600 nm (Pegau *et al.*, 1997). Since *Macrocystis* and *Nereocystis* are spectrally similar to one another in the NIR region (Cavanaugh *et al.*, 2010; Nijland *et al.*, 2019; Schroeder *et al.*, 2019a; Olmedo-Masat *et al.*, 2020), and the changes seen in the spectra of submerged kelp are due to properties of water absorption, we expect that the spectral results of this experiment are generally applicable to both *Macrocystis* and *Nereocystis* canopies, making these findings relevant for surface-canopy forming kelp species globally.

The results of these experiments were generally in line with our expectations according to similar studies of submerged aquatic vegetation (Kearney *et al.*, 2009; Turpie, 2013), although there were some interesting phenomena seen in the spectra that are worth noting. In the visible region of the spectra, R_{0+} in the red wavelength range decreased with depth, as expected. However, the R_{0+} at the absorption feature between 400 and 550 nm increased slightly with submersion. We hypothesize that this increase in R_{0+} is due to the scattering of light by the conditions of the water optical constituents, thus increasing the R_{0+} with depth. As such, we suspect that this increase in R_{0+} may be specific to the water conditions during the experiment and may not have occurred if the water had contained more optical constituents that absorb blue light, such as colored dissolved organic matter. Another interesting phenomenon noted in the floating kelp spectra was what appeared to be a sunlight-induced chlorophyll fluorescence (SICF) peak at 761 nm (Figure 4). Within the NIR region, photosynthetic organisms generally have a broad SICF peak centered at 740 nm (Meroni *et al.*, 2009). However, due to the high magnitude of the NIR reflectance, the SICF is usually only visible as a small, narrow peak centered at 761 nm. Typically, the R_{0+} within the NIR wavelength range overwhelms the signal from SICF, however, atmospheric gasses highly absorb incoming irradiance at 761 nm, which can create a fill-in effect by the SICF in this region (Meroni *et al.*, 2009). While this phenomenon has been correlated with photosynthetic output and general health of terrestrial vegetation and phytoplankton (Meroni *et al.*, 2009; Lu *et al.*, 2016), we are not aware of any publications that report an SICF peak in kelp spectra, and this may present an opportunity for future hyperspectral research. Once kelp was submerged the SICF feature was dampened, and therefore future research should take note of the amount of kelp at the surface if attempting to derive information from an SICF peak.

2.5.2 NIR Differences between Nereocystis Bulbs and Blades

The magnitude of reflectance across the NIR region in vegetation is generally due to the cellular structure of the respective tissues (Knipling, 1970). Both *Nereocystis* bulb and blade tissues are composed of the same three cellular layers: the meristoderm, the medulla, and the cortex. The meristoderm is a thin chloroplast-packed epidermal layer that surrounds the entire individual (Nicholson, 1970), and the medulla is a complex web of filaments that acts as a transportation system within the kelp, composing the innermost layer of kelp tissue (Nicholson, 1976; Schmitz & Srivastava, 1976). Between these two layers is the cortex, which connects the meristoderm to the medulla, and generally provides structural support for the kelp (Nicholson, 1970; Nicholson & Briggs, 1972). Given this structural arrangement, we speculate that the NIR signal from bulbs is consistently higher compared to the blades' signal because (1) the bulb cortex is many times thicker than the blade cortex (Nicholson & Briggs, 1972; Nicholson, 1976); and (2) the gas cavity of the bulb is lined by the medulla (Nicholson, 1976), creating a high surface area with many large refractive differences—similar to the mesophyll layer of a terrestrial leaf (Knipling, 1970; Slaton *et al.*, 2001). In comparison, the blade medulla is housed in a gelatinous extracellular matrix between cells (Nicholson, 1976), and with no gas cavities, the refractive differences are much smaller, allowing for increased transmittance of NIR light through the blades (Knipling, 1970). For our experiment, spectral measurements for blades were taken using a single blade wrapped around the polyethylene frame with only slight overlap between the edges of the blade. However, *Nereocystis* individuals may have between 30–60 blades each. Overall, a thicker mass of blade tissues due to high overlap may result in higher R_{0+} in the RE and NIR wavelength ranges than seen in this experiment.

2.5.3 The Implications of VI_n Saturation for Detection of Floating and Submerged Kelp

When the density or biomass of the vegetation increases within a pixel of remote sensing imagery, the VI_n for that pixel will asymptotically approach a saturation (i.e., a high VI_n value) (Tucker, 1979; Mutanga & Skidmore, 2004). This happens because when vegetation is dense, the R_{0+} at band 2 (NIR or RE) is large relative to the R_{0+} at band 1 (the visible band). Our spectral measurements contained 100% kelp within the field of view, and accordingly, the VI_n values calculated from the multispectral simulations were saturated when kelp was at the surface. Therefore, it is critical to understand how saturation affected the VI_n values of floating kelp, as well as when kelp was submerged. For example, our WV3 simulations for bulbs at the surface showed that the R_{0+} at NIR and RE bands were large compared to the red band (21%, 14%, and 1%, respectively). As such, both NIR_R and RE_R indices for bulbs at the surface were approaching saturation (0.83 and 0.77 respectively) and either index would perform relatively well for detecting floating kelp if a VI_n of zero was used as a threshold to classify kelp and water. When the bulb was submerged, the R_{0+} in the NIR and RE bands decreased rapidly by 10 cm depth (3.2 and 3.4% respectively) but were still relatively high compared to the red band, which had also decreased (0.6%), and therefore the NIR_R and RE_R values (0.66 and 0.68 respectively) were still relatively saturated, despite the large decreases in R_{0+} at the RE and NIR bands (Figure 5). As the kelp continued to be submerged, the R_{0+} at the NIR, RE, and red bands all continued to decrease, however, the R_{0+} at the NIR band decreased at a faster rate and therefore the NIR_R value dropped below the threshold of zero by 50 cm while the RE_R value was still above the threshold by 100 cm. Ultimately, this example shows that due to VI_n saturation, the choice of RE or NIR will make little to no difference in classification of kelp at or near the surface. However, once submerged, the use of an RE VI_n will still detect kelp deeper than an NIR VI_n.

2.5.4 Depth-detection Limits and Separability between Kelp and Water

While it is important to understand how VI_n values change as kelp is submerged, ultimately the accuracy of submerged kelp classification depends on the spectral separability between the submerged kelp and water. Here, we defined the depth at which kelp and water were no longer separable as the depth at where VI_n values for submerged kelp decreased below the threshold value. RE VI_n values for kelp and water had higher separability at deeper depths than their NIR counterparts (Figure 6), meaning that deeper kelp can be accurately classified when using an RE VI_n. Higher separability between kelp and water classes when using RE VI_n has been documented using both high spatial-resolution multispectral UAV imagery (Cavanaugh *et al.*, 2021a) and with moderate spatial-resolution multispectral satellite imagery of *Macrocystis* (Mora-Soto *et al.*, 2020), indicating that slight submergence of kelp surface-canopy may play a larger role in detection than previously thought.

While the choice between RE and NIR VI_n was an important factor in submerged kelp detection, the choice of the visible band can also shift the detection limits of submerged kelp. Our results show that both the water and submerged kelp spectra had higher R_{0+} in the green and blue wavelength ranges than in the red, and as such, submerged kelp became undetectable at shallower depths when using NIR_R compared to NIR_G or NIR_B. In the visible wavelength ranges, red is absorbed fastest by the water column, and in our experiment, the NIR signal is generally absorbed by around 50 cm depth, making it reasonable for this pairing to consistently have the shallowest detection limits for submerged kelp. At depths where the RE or NIR signal of kelp can no longer be detected, Figure 7 shows that subtle differences between kelp and water in the blue and green bands can still result in the kelp signal remaining above the dynamic threshold. However, these differences are small, and because conditions during the experiment

were controlled, the added spectral noise from in situ environmental factors would likely complicate the detection of both surface and submerged kelp in more realistic situations. For example, the blue wavelength ranges can be highly compromised in remote sensing imagery (Morel & Prieur, 1977; Mobley, 1994), with local variation in atmospheric composition reducing the certainty of accuracy for blue band values. Additionally, the optical constituents of coastal water can be highly spatiotemporally variable—affecting all regions of the spectra (Morel & Prieur, 1977; Phillips & Costa, 2017). At high concentrations phytoplankton in the water column may result in changes to reflectance in the visible wavelength ranges as well as high RE or NIR reflectance (Gower *et al.*, 1999), while changes to optical constituents such as sediment or CDOM may also impede the detection of submerged kelp (O'Neill *et al.*, 2011; Vahtmäe *et al.*, 2020).

In this experiment, the optical water conditions (Secchi = 7.5) were typical of the coastal waters of British Columbia (O'Neill & Costa, 2013; Phillips & Costa, 2017; Schroeder *et al.*, 2019a). Considering the Secchi measurement, the local depth (12 m), and the R_{0+} from water with no kelp (Figure 3), the bottom substrate signal was not part of the measured R_{0+} in our experiment. Yet kelp on the coast of British Columbia is often found as fringing canopies near the shoreline (Schroeder *et al.*, 2019a), which can result in a strong contribution of benthic substrate to the R_{0+} measured by space and air-borne platforms. Reflectance from shallow benthic features can result in highly variable R_{0+} in both the visible and near-infrared wavelength ranges, resulting in misclassification of submerged vegetation as canopy kelp (O'Neill & Costa, 2013; Vahtmäe *et al.*, 2020). Therefore, it is important to understand site characteristics (e.g., bathymetry and water turbidity) to define better the use of NIR or RE for kelp classification. For instance, if enough understanding of the local conditions at the time of imagery acquisition is not available, it may

be more appropriate to use NIR_R to reduce the addition of signal of the bottom substrate. Alternately, if imagery or associated ground truth data have a high enough spatial resolution (e.g., from UAV or other aerial platforms), visual interpretation of surface-canopy morphology from expert knowledge may be adequate for manual classification or ground truthing when using an RE VI_n.

2.5.5 Implications for Mixed Pixels

During the experiment, spectral data were collected using a small footprint to reduce uncertainties associated with having the reflectance signal of multiple targets within the field of view (i.e., mixed pixels). However, remote sensing imagery often contains mixed pixels (Cavanaugh *et al.*, 2011; Schroeder *et al.*, 2019b). This becomes especially problematic when sensors have a lower spatial resolution, where erroneous classification of a pixel as kelp may result in the overestimation of total kelp canopy. Multiple end-member spectral mixture analysis (MESMA) is an approach that has been applied to satellite imagery for both *Macrocystis* (Cavanaugh *et al.*, 2011; Bell *et al.*, 2020) and *Nereocystis* canopy (Hamilton *et al.*, 2020; Finger *et al.*, 2021) to determine what proportion of the pixel is kelp, and what proportion is water. When MESMA is applied to remote sensing imagery for kelp detection, it is assumed that all VI_n or band values within a pixel are a linear combination of kelp and water end-members (Cavanaugh *et al.*, 2011). However, if the kelp fraction within a pixel is low enough, the spectral contribution from water may overwhelm the kelp signal, lowering the overall pixel value and allowing the pixel to be erroneously classified as water (Nijland *et al.*, 2019; Hamilton *et al.*, 2020). Our results suggest that if submerged kelp is present when MESMA is performed, which is most often the case, the reduced signal from the submerged kelp within the pixel may lead to

an underestimation of the kelp fraction within the pixel. Using an RE VI_n when performing MESMA may allow the user to detect more submerged kelp, thus contributing to a higher overall pixel value and increasing the accuracy of the classification. This may be especially relevant if attempting to determine relationships between remote sensing imagery and biomass, since *Nereocystis* blades show a higher correlation to the mass of the individual than any other metric tested (Stekoll *et al.*, 2006). Further, *Nereocystis* canopy generally has less dense biomass at the surface than *Macrocystis* (Sutherland, 1990; Finger *et al.*, 2021), and, therefore, is more likely to be misclassified in moderate or low spatial resolution imagery.

2.6. Conclusion

Our experiment contributes new, detailed information on the effects of kelp submersion on the above water reflectance, as well as a comparison of the depth detection limits of kelp when using red-edge and near-infrared indices. We determined that the near-infrared region of kelp spectra is strongly absorbed upon submersion, however, there is a narrow spectral peak in the red-edge region that can be used to enhance the remote sensor's ability to detect submerged kelp due to lower water absorption. Detection limits varied based on kelp tissue, the thresholding method, and the visible band used in the vegetation index calculation, but overall, red-edge vegetation indices detected deeper than their counterpart NIR indices, which may allow the remote sensor to improve accuracy when mapping sparse and partially submerged kelp canopy or attempting to derive biomass from canopy reflectance values. Kelp forests may be mapped using remote sensing for various reasons, ranging from estimation of biomass for kelp harvesting to multi-year temporal analyses to assess the impacts of environmental drivers on kelp ecosystems. Yet kelp systems can be highly variable in abundance between years, and our study shows that the spectral variables used to detect kelp canopy in remote sensing imagery play an important role in

the amount of submerged kelp canopy detected. Therefore, it is critical for a remote sensing user to understand how the physical interaction between light and water may affect the depth at which kelp can be detected. For example, RE VIn might be especially useful if resource managers are attempting to set quotas for harvestable biomass of *Nereocystis* and wish to detect as much blade biomass as possible for specific beds. However, if one wishes to reduce detection of subsurface kelp canopy or other shallow benthic vegetation, we recommend the use of the NIR_R (NDVI), which consistently had the shallowest detection limits of the indices tested.

3.0 Understanding the Uncertainties Associated with the Remote Sensing of Morphologically Distinct Kelp Canopies at Different Tidal Heights and Current Speeds.

3.1 Abstract

Remote sensing is a key tool for monitoring the surface-canopy extent of nearshore kelp forests (*Macrocystis pyrifera* and *Nereocystis luetkeana*) along the Northeast Pacific coast. *Macrocystis* and *Nereocystis* species are morphologically distinct, which impacts the *in situ* spectral signatures of their canopies and the ability to detect those canopies with remote sensing as they are submerged by tides and currents. In this study, hyperspectral data from an ASD Fieldspec Handheld-2 spectroradiometer (325-1075 nm) and multispectral data from a DJI Phantom 4-Multispectral unoccupied aerial vehicle (UAV) were used to characterize the *in situ* spectral and spatial differences between *Macrocystis* and *Nereocystis* surface-canopy structures. Multispectral UAV imagery was collected to examine the effects of tides and currents on the surface-canopy extent of both *Macrocystis* and *Nereocystis.* We tested differences in surface area classifications between two vegetation indices: the normalized difference red-edge (NDRE) and normalized difference vegetation index (NDVI). *In situ* hyperspectral data showed that submerged surface-canopy structures had a higher reflectance in the red-edge than the near-infrared and UAV imagery classified with NDRE detected roughly 18% more surface-canopy in total than with imagery classified with NDVI. At low-current sites (<10cm/s), the surface-canopy area detected with UAV imagery decreased by an average of 22.5% per meter of tidal increase, regardless of species present. However, *Nereocystis* surface-canopy at the high-current site (>10cm/s) decreased at nearly twice the average rate of kelp beds at the low-current sites. We suggest that outside of specifically high current regions, a predictable linear relationship between detected

surface-canopy area and tidal height can be used to understand potential errors when using remote sensing imagery collected at different tidal heights to monitor kelp on a regional scale.

3.2 Introduction

Kelp forests are highly-productive marine ecosystems that provide numerous ecologically and commercially important ecosystem services (Mann, 1973; Krumhansl & Scheibling, 2012). In recent decades, some kelp forests have undergone large reductions and even extirpation, making it important to monitor changes in these vital ecosystems (Krumhansl *et al.*, 2016; Wernberg *et al.*, 2019). In the Northeast Pacific, *Macrocystis pyrifera* (giant kelp) and *Nereocystis luetkeana* (bull kelp) are two important kelp species that form morphologically distinct surface canopies that can be monitored using remote sensing methodologies (Pfister *et al.*, 2017; Nijland *et al.*, 2019; Schroeder *et al.*, 2019b; Cavanaugh *et al.*, 2021a). Measuring changes to the surface-canopy area of kelps from aerial and satellite imagery can be used to understand how environmental drivers, such as inter-annual and decadal climate regimes (Pfister *et al.*, 2017; Schroeder *et al.*, 2019a; Bell *et al.*, 2020), or pulse events like marine heatwaves (Arafeh-Dalmau *et al.*, 2019) influence the spatial and temporal persistence of kelp forests.

Kelp and water can be distinguished in remotely sensed imagery by taking advantage of the kelp surface-canopy's high reflectance in the near-infrared (NIR) region (700-100 nm) and the surrounding water's low NIR reflectance (Jensen, 1980; Schroeder *et al.*, 2019b). However, *in situ* oceanographic and biological conditions at the time of imagery acquisition can cause uncertainties when mapping kelp forests with remote sensing imagery. For example, portions of the canopy may be submerged by changing tides and tidal currents (Britton-Simmons *et al.*, 2008; Cavanaugh *et al.*, 2021b) or simply due to the morphological differences in surface-canopy structures and the position of those structures at the water's surface (Schroeder *et al.*,

2019b). When kelp canopy is submerged, the above-water spectral signal of the kelp and water are combined, and the high NIR signal of kelp is dampened by the absorption by water, potentially reducing the area of surface-canopy detectable from above water (Augenstein *et al.*, 1991; Schroeder *et al.*, 2019b; Cavanaugh *et al.*, 2021b).

To minimize issues related to canopy submersion that may occur when tidal heights change for different imagery acquisition, the general recommendation is to use imagery collected at low tidal heights, when the maximum extent of kelp canopy is detectable at the surface (Pfister *et al.*, 2017; Nijland *et al.*, 2019; Schroeder *et al.*, 2019a; Hamilton *et al.*, 2020). Yet, tidal ranges vary for different regions, and acquiring cloud-free imagery during low tide is not always possible, especially northward from California to Alaska (Cavanaugh *et al.*, 2021a), where increases in tidal range and frequency of cloud cover may limit the availability of low-tide imagery in some areas. In order to adjust for variability in kelp extent with submergence, it is important to quantify the relationship between surface-canopy area and tidal height (Stekoll *et al.*, 2006). Further, even if all imagery are acquired within a narrow tidal range, there can still be substantial variability in detected kelp area extent between images based on differences in the rate of submersion between the species or ecotypes being monitored in a region (Britton-Simmons *et al.*, 2008; Cavanaugh *et al.*, 2021b), the presence of optically active water components like chlorophyll or suspended sediments (Mobley, 1994), or differences in the intensity of local currents within a region (Britton-Simmons *et al.*, 2008).

Beyond the uncertainties caused by *in situ* oceanographic and biological conditions, there are differences in the methods used to estimate the area of kelp surface-canopy, such as the use of different spectral bands or wavelengths for kelp classification, that can also cause uncertainties when mapping kelp (Augenstein *et al.*, 1991; Schroeder *et al.*, 2019b; Cavanaugh *et al.*, 2021b).

For instance, in coastal waters, light absorption is generally the lowest in the visible wavelengths and increases exponentially at longer wavelengths (Mobley, 1994). Therefore, wavelengths in the longer NIR ranges (> 800 nm) are subject to higher absorption than wavelengths in the red-edge (RE) range (670-750 nm).

The lower absorption of RE wavelengths versus longer NIR wavelengths means that RE wavelengths can penetrate deeper in the water, allowing for deeper kelp detection in the water column than with longer NIR wavelengths (see chapter 2 results). The use of RE bands in vegetation indices have been shown to slightly improve the separability between *Macrocystis* surface-canopy and water in satellite and UAV imagery (Mora-Soto *et al.*, 2020; Cavanaugh *et al.*, 2021b). However, older satellite sensors used to map kelp were not designed to measure reflectance at RE wavelengths, and many sensors only have a single NIR band (e.g., Landsat series, SPOT series) (Tucker, 1978; Barsi *et al.*, 2014; Schroeder *et al.*, 2019b). As such, long-term remote sensing studies that use archived imagery generally focus on the NIR bands for kelp classification, often using the normalized difference vegetation index (NDVI) to enhance kelp detection based on differences in the NIR and red wavelengths, similar to terrestrial vegetation (Jensen, 1980; Nijland *et al.*, 2019; Schroeder *et al.*, 2019b; Hamilton *et al.*, 2020; Bell *et al.*, 2020; Butler *et al.*, 2020).

Overall, there are numerous sources of uncertainties related to mapping kelp surface canopy with remote sensing. Often morphological differences between species are undetectable due to lack of spatial resolution (Nijland *et al.*, 2019; Mora-Soto *et al.*, 2020), and the apparent area of kelp beds in remote sensing imagery may change depending on local tides and currents (Britton-Simmons *et al.*, 2008; Cavanaugh *et al.*, 2021b). Here, our goal was to better understand uncertainties that may arise due to submersion of kelp canopy, when using remote sensing

imagery for mapping kelp aerial extent. To address this goal, (i) we characterized the spectral differences between *Nereocystis* and *Macrocystis* surface-canopy structures using both *in situ* hyperspectral measurements and multispectral UAV imagery, and (ii) we investigated the relationship between the surface-canopy areas of both *Nereocystis* and *Macrocystis* with tidal height and current speed, using tide and current data from an acoustic Doppler current profiler; and, we further compared these results using both RE and NIR vegetation indices derived from multispectral UAV imagery. This work contributes to a global effort to monitor surface-canopy forming kelp by detailing the first direct comparison of the *in situ* above-water spectral signatures of *Nereocystis* and *Macrocystis* surface-canopy structures. It also adds to the limited scientific knowledge on how both species' canopy structures respond to submergence by tides and associated tidal currents, and how this information contributes to variability and uncertainty in remote sensing measurements of kelp extent.

3.3 Methods

3.3.1 Study Sites

This research was conducted at six sites located near the Hakai Institute ecological field station on Calvert Island (51°39′16″N 128°07′53″W) on the Central Coast of British Columbia over two weeks in July, 2020 (Figure 9). The region is characterized by a complex coastline with numerous channels, fjords, and islands, creating a mosaic of habitats for aquatic vegetation (Nijland *et al.*, 2019; Olson *et al.*, 2019). Mean sea surface temperatures range from 7°C to 15°C annually (Jackson *et al.*, 2015), and tides in the region are semidiurnal, with tidal exchanges ranging between 3 to 5 meters (Thomson, 1981). The two dominant surface-canopy forming kelp species are *Macrocystis pyrifera* and *Nereocystis luetkeana*, both of which can be found in both mono-specific and/or mixed beds (Sutherland, 2008; Nijland *et al.*, 2019). Although species-level abundance data are uncommon for this region, aerial surveys conducted by the government

of British Columbia show that between 1993 and 2007, a major shift occurred from *Nereocystis* to *Macrocystis* dominated reefs (Sutherland, 2008), and since then, shifts in kelp abundance have occurred locally at different sites, likely as a result of trophic cascades (Burt *et al.*, 2018) and climatic shifts (Krumhansl *et al.*, 2016).

To account for site variability the placement of kelp beds along the heterogenous coastline, we surveyed a range of site types (e.g., bays, channels, headlands) across various conditions (e.g., exposure, current speeds) that included both *Macrocystis* and *Nereocystis* beds, with site selection based on expert knowledge from the Hakai Institute's kelp monitoring program. Our chosen locations required: (1) distinct kelp beds that an unoccupied aerial vehicle (UAV) could collect imagery of within a single flight, (2) a relatively flat subtidal benthos near the kelp bed for the benthic placement of an acoustic doppler current profiler (ADCP) to collect concurrent tide and current data; and (3) a nearby shoreline that could be captured in imagery and used for georeferencing UAV images. Two of the sites (Triquetta and Starfish) contained two distinct kelp beds within the UAV flight path, therefore eight beds were analyzed even though only six sites were surveyed: four *Macrocystis*, three *Nereocystis*, and one mixed bed site. Each distinct bed was given its own code (Table 3, Figure 9). The bathymetric extent of all kelp beds were between 0 to -5m (LLWLT) according to high resolution local bathymetric data supplied by the Hakai Institute.

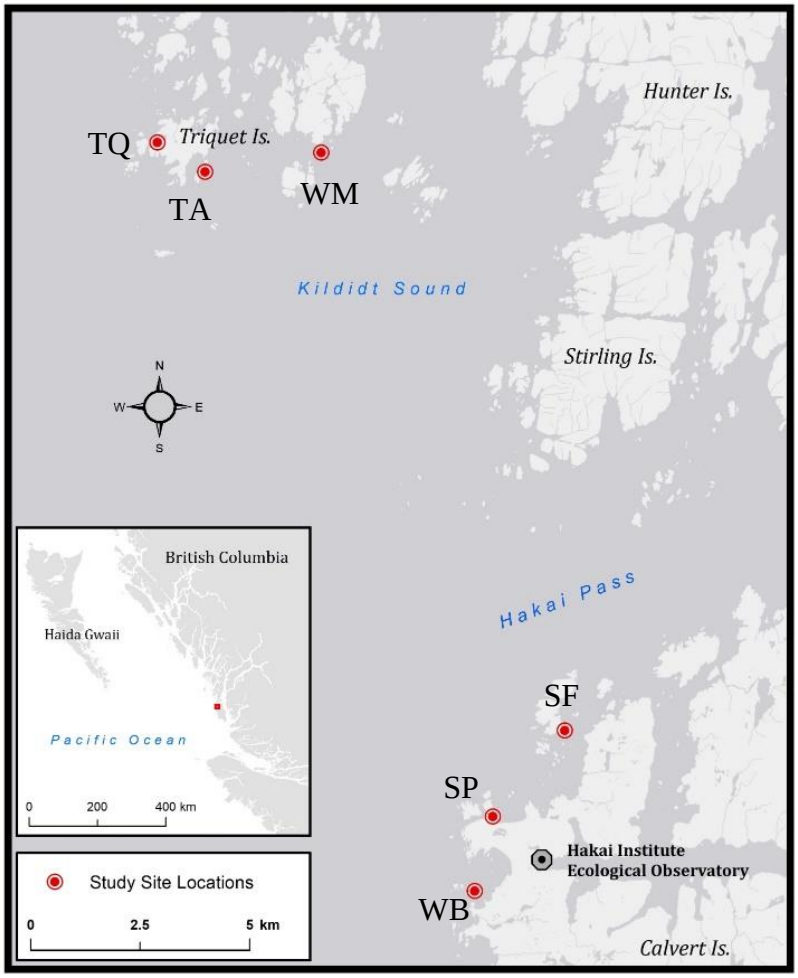

Figure 8. Study site locations on the Central Coast of British Columbia. TQ = Triquet Bay, TA = Triquetta, WM = Womanley, SF = Starfish Channel, SP = Surf Pass, WB = Westbeach

Table 6. List of codes used for each bed surveyed, according to site and species present.

Bed code	Site	Species
TQ	Triquet	*Macrocystis*
SF_N	Starfish	*Nereocystis*
SF_M	Starfish	*Macrocystis*
WB	Westbeach	*Macrocystis*
WM	Womanley	*Macrocystis*
TA_1	Triquetta	*Nereocystis*
TA_2	Triquetta	*Nereocystis*
SP	Surf Pass	Mixed

The buoyancy of kelp surface-canopies is directly related to their morphology (Burnett & Koehl, 2017). For example, the pneumatocyst and blades of *Nereocystis* sit differently at the surface of the water from one another; the pneumatocyst being positively buoyant and the blades negatively buoyant. The pneumatocyst is a single elongated gas bladder that is anchored to the benthos by a stipe and holdfast. Between 30-60 blades, which are often around four meters long, trail from the distal end of the pneumatocyst (Springer *et al.*, 2007; Koehl *et al.*, 2008), and while the blades are negatively buoyant, they are often held aloft in the water column by passing currents (Koehl *et al.*, 2008). In comparison, the *Macrocystis* surface-canopy is composed of multiple structures often referred to collectively as fronds. Fronds are made up of numerous thin stipes rising from a large holdfast on the sea floor, with each stipe lined with many small buoyant pneumatocysts and a single negatively buoyant blade protruding from the distal end of each pneumatocyst (Druehl & Wheeler, 1986). The combined buoyancy of the many small pneumatocysts holds the fronds at the surface, but the individual parts of the frond (e.g. blade vs stipe vs pneumatocyst) are not large enough or spatially separated from one another to discern independently, even in reasonably high-resolution remote sensing imagery compared to *Nereocystis* pneumatocysts and blades (Finger *et al.*, 2021). The total amount of kelp tissue that is emergent at the water surface will ultimately depend on the combined positive and negative buoyant forces acting on the individual for each of these structure types.

3.3.2 Data Collection and Processing

3.3.2.1 *In situ* above-water reflectance

To characterize the *in situ* spectral differences between *Macrocystis* fronds, *Nereocystis* pneumatocysts, and *Nereocystis* blades, *in situ* above-water spectra were collected for dense samples of each kelp structure type using the ASD Fieldspec Handheld 2 spectroradiometer

(325-1075 nm) aboard a 22’ aluminum motor vessel. Black fabric was placed across the side of the vessel to minimize spectral reflection off the boat onto the water/kelp reflectance signal during acquisition, and the boat was positioned to avoid shadowing of the targets (Schroeder *et al.*, 2019b). Above-water spectra were also collected over optically deep water at each site, except for Surf Pass, due to technical problems with the spectroradiometer that day. For each spectral target, 10 consecutive radiance measurements (L_T) were collected at one metre above the water at a viewing angle of 40° from the nadir and a sensor-sun azimuthal angle of 135° (Mobley et al., 1999). With a 10° fore-optic, the spectroradiometer detected a target footprint roughly 20 cm in diameter on the surface. A Sony HDR-AS50 digital camera mounted on the ASD spectroradiometer was used to collect a matching image for each spectral target acquired. Before acquiring spectra for each target, white reference (L_{spec}) and dark-current readings were taken for calculating reflectance and reducing noise in the hyperspectral data, respectively (ASD, 2017). Wavelength dependant above-water hyperspectral reflectance ($R(\lambda)_{0+}(\%)$), hereafter R_{0+}, was derived from the L_T and L_{spec} radiance measurements for each target (Equation 3)(Mobley, 1994; ASD, 2017).

$$R(\lambda)_{0+}(\%) = \left(\frac{(L_T(\lambda))}{(L_{spec}(\lambda))}\right) \times 100 \qquad (3)$$

Spectral data were collected opportunistically across several days of field work under varying environmental conditions, and data collected while skies were overcast had an increase of roughly 3-5% R_{0+} across the spectra due to the reflection of clouds as glint on the water’s surface (Kutser *et al.*, 2013) compared to clear, cloud-free days. Therefore, to compare spectral features from different survey dates, all kelp spectra were normalized at 500 nm, and all water spectra were normalized using the lowest R_{0+} value between 850-900 nm. No sky corrections were

conducted specific to the blue region; however, our analysis of the hyperspectral and UAV data only used the red, RE, and NIR bands, where the effects of sky radiance on the water surface are relatively small (Karpouzli & Malthus, 2003). Normalized R_{0+} measurements for kelp were simulated into the red, RE, and NIR bands of the DJI Phantom 4-Multispectral UAV using Gaussian functions with the sensor's spectral response for each band, and these bands were used to calculate normalized vegetation indices (VI_n; Equation 4).

$$VI_n = \frac{band\ 2 - band\ 1}{band\ 2 + band\ 1} \quad (4)$$

Here, we used NDVI, where band 2 = NIR and band 1 = red, and a 'normalized difference red-edge' index (NDRE), where band 2 = RE and band 1 = red. NDVI is a commonly used vegetation index in kelp mapping (Jensen, 1980; Nijland *et al.*, 2019; Schroeder *et al.*, 2019b,a; Hamilton *et al.*, 2020; Bell *et al.*, 2020; Butler *et al.*, 2020), and NDRE is similar but uses the RE band instead of the NIR band. We chose NDRE instead of NDREB (like Cavanaugh *et al*., 2021b, who used the blue instead of the red band) due to the lower influence of sky radiance in the red region of the electromagnetic spectrum, and also to minimize differences between VI_n values due to differences in the visible portion of the spectrum. However, when the RE or NIR band values are high relative to the visible band in a VI_n, the VI_n value can become saturated and spectral information may be lost (see section 2.5.3). Therefore, to better understand the strength of the signal in both the RE and NIR regions of kelp canopy, the ratios between the simulated RE and NIR band values of the multispectral UAV as well as the calculated NDRE and NDVI from simulated band values were compared for each structure type.

3.2.2.2 UAV imagery

Multispectral imagery was collected using a DJI Phantom 4-Multispectral UAV, which carries six 1/2.9" CMOS sensors, each with a 62.7° field of view. One of the sensors captures RGB imagery, which was not used here, and the other five sensors are monochromatic, capturing blue (450 nm ± 16 nm), green (560 nm ± 16 nm), red (650 nm ± 16 nm), red-edge (730 nm ± 16 nm), and near-infrared (840 nm ± 26 nm) images (DJI, 2019). Fifty-one flights were conducted over six days at six sites between the daily range of tidal heights at 0.5 meter intervals. Flights were conducted at a standard height of 90 metres above sea level with a ground sample distance (i.e., pixel size) of approximately 5 cm. Flight paths had 80% side-lap and 80% front lap between images to maximize the number of features available to be used as tie points during the orthomosaic creation. The P4MS has a downwelling light sensor that collects *in situ* irradiance data during flights, and before and after each flight, an image was manually collected from a panel of known reflectance to aid in sensor calibration during the orthomosaic creation process. Wind speed was collected using an anemometer at the beginning of each flight and generally remained below 5 m/s during all surveys; however, daily site selection was partially based on placement of kelp beds on the leeward side of the shoreline, and therefore wind speeds detected from the boat likely had less of a disturbance on the water surface than might be expected in open water or exposed areas (Nahirnick *et al.*, 2019b,a).

The Canadian chart datum of lower low water large tides (LLWLT) were used to plan all UAV flights, rather than the mean lower low water (MLLW) chart datum used in the U.S.A. LLWLT are calculated by averaging each of the lowest predicted annual low water values over a 19-year tidal epoch, while MLLW are calculated by averaging the daily observed low water values over a 19-year tidal epoch (Forrester, 1983). Although differences between these chart data vary at

different locations across the coast, 0 m MLLW is vertically higher on the shoreline relative to 0 m LLWLT, and therefore our tidal heights of 0 m would be consistently negative values using the MLLW chart datum (Forrester, 1983); an important distinction for the comparison of our results with those of other studies (e.g. Hamilton *et al.*, 2020; Cavanaugh *et al.*, 2021).

3.3.2.3 Biophysical water properties

For each survey, in addition to above-water spectra, additional metrics of the daily variability of optical constituents in the water were collected. Characterizing *in situ* optical constituents is important because the detection of kelp is based on the ability to separate the spectral signatures of kelp and water (Jensen, 1980), and, locally, the spectral signature of water can vary both spatially and temporally (Phillips & Costa, 2017). Hyperspectral downwelling irradiance data were collected with a Satlantic Hyperpro in-water profiler, and used to calculate the diffuse attenuation coefficient (K_d) between 400-800nm within the top one meter of the water column following the methods outlined by O'Neill *et al*. (2011) and Satlantic (2012). The K_d is a wavelength dependent measurement that quantifies the spectral decrease in light energy as a function of depth (Hooker & Maritorena, 2000; Dekker *et al.*, 2005). K_d was calculated for each site except for Westbeach, due to technical problems that day. In addition, Secchi depth was measured, and water samples were collected in triplicate each day to quantify total suspended matter (TSM), as well as percent organic matter (POM) and percent inorganic matter (PIM) of the TSM using the loss of weight on ignition method (Byers *et al.*, 1978; Heiri *et al.*, 2001; Phillips & Costa, 2017). Together with the above-water spectra, the K_d, TSM, POM, and PIM informed on the range and variability of water optical constituents and Secchi depth measurements quantify the general water clarity (Preisendorfer, 1986) between days and sites.

A 12kHz Workhorse Sentinel acoustic Doppler current profiler (ADCP) was deployed on the seafloor facing upward each day during UAV surveys, allowing for simultaneous and continuous *in situ* depth and current measurements during each UAV flight (Figure 11). Due to ADCP requirements for depth, pitch, and roll of the unit, as well as the distance from moving vegetation that might impede the beams (RD Instruments, 2005), the ADCP was strategically placed adjacent to the kelp beds in a location that would generally characterize the currents within each site. All tidal height and current data from the ADCP were processed with current speed (cm/s) calculated as a non-directional absolute value on a horizontal axis between 0.5 to 1.5 metres depth and averaged into 10 minute periods.

3.3.2.4 UAV Imagery Processing

Before assessing the kelp in the UAV imagery, (1) glint masks were created for imagery that contained glint and (2) orthomosaics were created to stitch imagery together at the site level. Next, (3) kelp beds were isolated within the orthomosaics and both NDRE and NDVI VI_n rasters were created for each isolated kelp bed. Finally, (4) Jenks Natural breaks were used to classify kelp and water within each VI_n raster.

Orthomosaics of each site were created using a Structure from Motion Multi-View Stereo (SfM-MVS) workflow within Agisoft Metashape photogrammetry software. In the SfM-MVS workflow, common points (individual terrain features) are identified from multiple overlapping images, such as the shoreline, benthic features, and kelp canopy, to create tie points (Aasen et al., 2018; Taddia et al., 2020). These “tie points” allow different images to be matched and the scene geometry reconstructed (i.e., generates a 3D model). The images are projected onto the 3D model to remove the perspective distortion from the images. The final product is a 2D

orthomosaic. In this study, all orthomosaics were georeferenced to a common raster to increase positional accuracy. Marine environments can be challenging to map using SfM-MVS because large open water areas are featureless which may leave an orthomosaic with gaps. This issue is exacerbated during high tides when more features in the scene are submerged and therefore obscured. The combination of cloud cover, solar elevation, and the texture of the water's surface during a UAV survey may result in the presence of sun glint in images. The presence of glint reduces the quality of the final orthomosaic and may result in the misclassification of glint as kelp (Cavanaugh *et al*., 2021b; Schroeder *et al*., 2019b). In this study, a protocol for masking glint in imagery was incorporated following methods developed by Cavanaugh *et al.* (2021b) and a tool created by Denouden et al. (2021). Due to other unfavourable conditions during UAV surveys, orthomosaics were not generated for four out of the fifty-one total flights: three at Triquetta (collected at 3.25 m - 4.25 m) and one at Westbeach (collected at 3.8 m). All orthomosaics were projected to the geographical coordinate system, NAD 1983 UTM zone 9N, resampled to 5 cm x 5 cm pixels to ensure a standard resolution between all orthomosaics, and georeferenced to a single high-resolution aerial image of the study region.

At each site, a combination of Definiens eCognition and ESRI ArcMap were used to isolate a single area for each kelp bed. These areas contained outer edges of the kelp surface canopy from each flight at all tidal heights by removing land, deep water, and unwanted vegetation/understory from the orthomosaic (Figure 10a). After kelp beds were isolated, NDVI and NDRE VI_n rasters were calculated from the red, RE, and NIR band values of each image (Figure 10b). Histograms of VI_n values for each raster were bimodal representing kelp and water in the image at low tide, and a threshold based on the Jenks natural breaks feature in ARC-Map was defined to separately classify kelp and water. Jenks natural breaks classify the pixels of an image by selecting a

threshold in the frequency histogram of the image that reduces the variance within each class while maximizing the variance between classes (Jenks, 1977). Here, the Jenks function in ARC-Map placed the threshold for each image in the trough of the bimodal histogram values of kelp and water (Figure 10c). Despite changes to the histogram's shape as kelp tidal height increased and kelp was submerged (i.e., less kelp, more water), threshold values selected by Jenks breaks generally shifted less than 0.1 of a VI_n value between images over the course of a day, making it a robust and unbiased method of selecting a threshold. After classification, the surface-canopy area was calculated from each VI_n raster (Figure 10d).

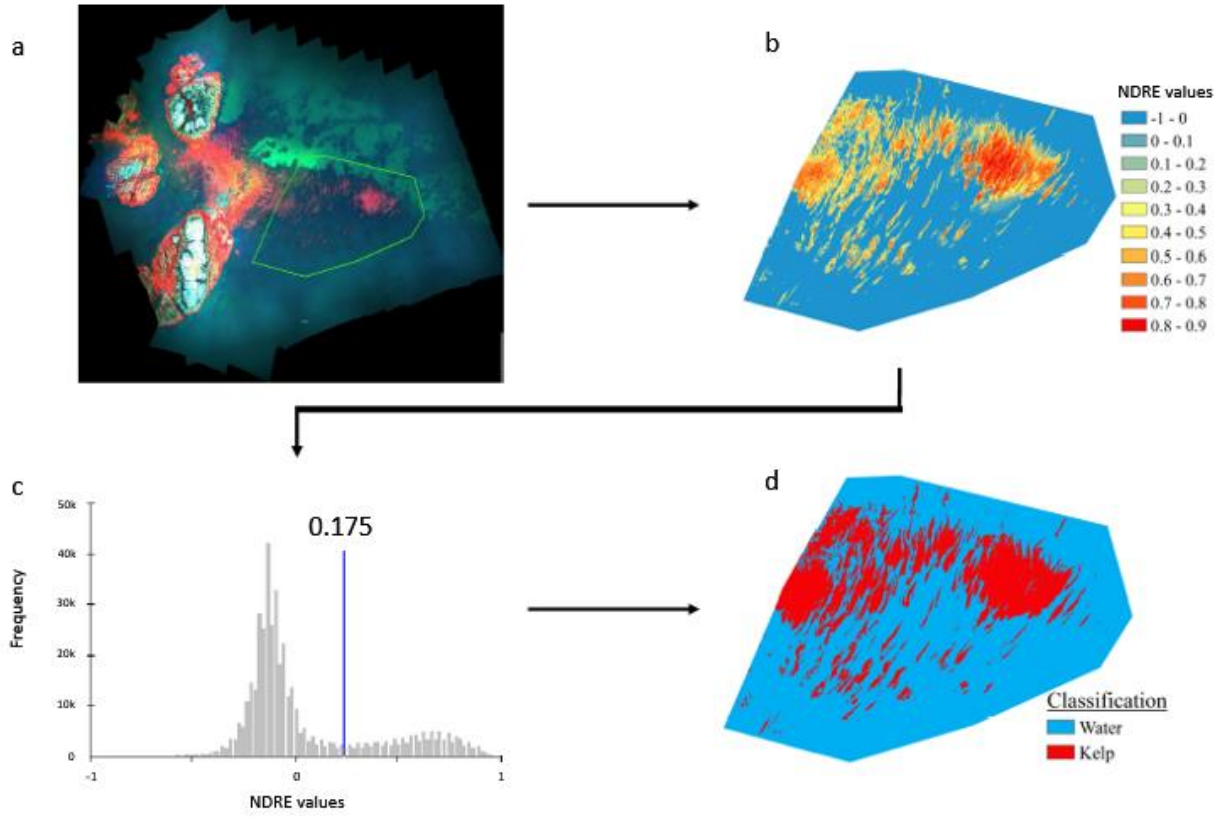

Figure 9. The kelp classification process, starting with a) the full orthomosaic with a green outline showing the isolated kelp bed used for analysis, b) the VI_n raster c) the frequency histogram of the image within the green outline showing the Jenks natural breaks threshold in the trough between the water (lower) and kelp (higher) peaks, and d) the resulting binary classification of kelp and water.

UAV flights were generally conducted under homogenous sky conditions (either completely sunny or completely overcast); however, during some flights variable cloud conditions resulted in large radiometric changes which affected the orthomosaic quality. In these cases, the VI_n raster was split in two segments, with kelp surface-canopy area being determined for each segment independently following the methods above. Afterwards, the two separately determined canopy areas from each segment were summed together, giving a single kelp area for the orthomosaic.

3.3.3 Statistical Analyses:

3.3.3.1 Evaluation of NDRE and NDVI for Kelp Classification in UAV Imagery

Prior to statistical comparisons, exploratory analysis of the data showed that in surveys where less than ~150 m^2 of kelp was detected (mostly in imagery collected at tides > 2 m), NDRE detected much more kelp than NDVI. This increase was an artifact of smaller beds at high tides becoming almost entirely submerged and mostly undetectable with NDVI. Since most kelp remote sensing imagery is collected at lower tides with beds much larger than 150 m^2 (e.g., a single Landsat pixel is 900 m^2), here, we only compared imagery with more than 150 m^2 of kelp extent. In total, imagery from 10 of the 65 total orthomosaics were removed with an average tidal height of 2.9 meters.

A pairwise t-test was used to compare the mean difference between NDRE and NDVI classified surface-canopy areas across all orthomosaics (Cohen, 1988). Then, to investigate whether these differences vary between *Macrocystis* and *Nereocystis* canopies or at high versus low tidal heights, the ratio between NDRE area and NDVI area was determined for each bed, and two separate analyses were conducted. A two-sample t-test was used to compare the average NDRE:NDVI ratio between *Nereocystis* and *Macrocystis* (Cohen, 1988), and a Welch's t-test was used to compare the average NDRE:NDVI ratio for surveys below a 2m tidal height with

surveys at or above a 2m tidal height (Cohen, 1988). For all comparisons, assumptions for normality were verified using the Shapiro-Wilk test and for equality of variance using an F-test (Cohen, 1988).

3.3.3.2 The Effects of Tidal Height and Current Speed on NDVI Classified Surface Canopy Area

In areas with a large tidal range, tidal height can significantly affect surface-canopy area estimates. However, the effects of current speed are less predictable and may not be noticeable if current speeds are low enough (Britton-Simmons *et al.*, 2008; Cavanaugh *et al.*, 2021b). Here, a separate multiple linear regression model was fit for each bed with the surface-canopy area as the dependent variable and tidal height and current speed as the independent variables to investigate whether currents were strong enough to have an effect on surface-canopy area (Faraway, 2002). NDVI surface-canopy area was chosen rather than NDRE for this portion of the analysis because NDVI is the most commonly used vegetation index for kelp remote sensing, and not all sensors have a RE band. Shapiro-Wilk tests were performed to determine normality of residuals for each model and variance inflation factors were calculated to quantify the level of correlation between tidal height and current speed at each site (Cohen, 1988; Stine, 1995). The multiple regression coefficients for each model were assessed for significance to determine whether the independent variables significantly improved the predictive power of the models (Faraway, 2002).

Nearshore currents can be completely decoupled from the general oceanographic currents within a region (Britton-Simmons *et al.*, 2008), making it challenging to acquire and incorporate current data when analyzing remote sensing imagery. Therefore, the relationships between tidal height (x) and NDVI classified kelp area (y) for each bed were defined using simple linear regression models (Equation 3), while ignoring *in situ* current speeds.

$$y = mx + b \quad (3)$$

Since kelp bed size varied between sites, tide-area relationships were standardized by dividing the slope of each linear equation (*m*) by the y-intercept (*b*), which provided the decrease in surface-canopy area per meter as a percentage of the estimated kelp area at 0 m tidal height LLWLT (Equation 4).

$$\text{Percentage of bed area decrease per meter (\%/m)} = \left(\frac{m}{b}\right) \times 100 \qquad (4)$$

This standardization relied on the assumption that all estimates of the y-intercept were reasonably accurate (see results section for r^2 values) and that the area at 0 m tidal height was a reasonable benchmark that represented 100% of possible kelp canopy at the surface. Beds were grouped by species as well as by high-current (> 10 cm/s) and low-current (< 10 cm/s) sites, and descriptive statistics were used to characterize the average values (mean $\pm$ SD) as well as the overall ranges of slopes for the area-tidal height relationships of each group (both current and species). In Section 3.5, the rates of mapped canopy decrease from this study are compared with other tide and current analyses. Here, since different authors use different methods to calculate percent changes, results from other authors were first standardized using our method (equation 4), and where American datum charts were used (MLLW), the y-intercept (*b*) was considered to be the lowest stated tidal height for the region, rather than 0m.

Since both kelp detection and biomass estimates are generally linked to the vegetation index value within a remote sensing pixel (Cavanaugh *et al*., 2010), it is important to understand the spatial trends of vegetation index values within a kelp bed at different tidal heights with high resolution satellite imagery. At the Womanley *Macrocystis* bed, five simulated 2 m x 2 m 'pixels' were overlayed one meter apart on three orthomosaics collected at low (0.2 m) , medium (1.7 m), and high (3.2 m) tidal height, to capture the range of index values across the kelp bed.

Within each pixel at each tidal height, the average values (mean ± sd) for NDVI and NDRE were calculated, and used to inform on the spatial variability of index values within a kelp bed.

3.4 Results

3.4.1 Spectral Characterization of Kelp and Water

The normalized R_{0+} of the *in situ* spectra for dense kelp structures (Figure 11a) showed that visible wavelengths between 500-700 nm overlapped one another, with similar peaks at 575, 600, and 645 nm regardless of structure (pneumatocyst, frond, or blade). Similarities in spectral shape between species were due to shared photosynthetic and accessory pigments, with both *Nereocystis* and *Macrocystis* species having a combination of chlorophyll-a, chlorophyll-c, and fucoxanthin pigments (Duncan, 1973; Wheeler, 1980). Spectra for all kelp structures showed an RE and NIR peak around 715 and 815 nm, respectively, however, the magnitude of the peaks varied in relation to each other depending on how the structure floated at the water surface (i.e., their buoyancy). *Nereocystis* pneumatocysts (Figure 11a-i) remained largely emergent above the water, and the NIR peak was larger relative to the RE peak, consequently the NIR/RE ratio of the simulated multispectral bands was 1.14. Both *Macrocystis* fronds (Figure 11a-ii) and *Nereocystis* blades (Figure 11a-iii) sat mostly just below the water surface and their RE peaks were larger relative to their NIR peaks, resulting in simulated multispectral NIR/RE band ratios of 0.88 and 0.44, respectively. The simulated NIR and RE band signals of *Nereocystis* pneumatocysts and *Macrocystis* fronds were much higher relative to the red band signal. Therefore, VI_n for both *Nereocystis* pneumatocysts (NDRE: 0.94, NDVI: 0.95) and *Macrocystis* fronds (NDRE: 0.91, NDVI: 0.90) were saturated (see section 2.5.3) and all VI_n values were similar for these structures despite differences in R_{0+} magnitude. Compared to the pneumatocysts and fronds, the overall NIR and RE band signals for *Nereocystis* blades were only slightly higher than the red band and as such, the VI_n values for blades (NDRE: 0.57, NDVI: 0.23) were much lower than

those of the other structures. In addition, the NDRE signal for *Nereocystis* blades was more than twice that of the NDVI signal.

The same patterns observed in the kelp spectra and their simulated indices were observed qualitatively in the false colour RGB DJI P4MS imagery of Macrocystis (Figure 11b) and Nereocystis (Figure 11c). In the colour combination displayed in Figure 11c, emergent Nereocystis pneumatocysts appear bright orange/yellow, indicating a higher signal in the NIR band than the RE band. Submerged Nereocystis blades appear green, indicating a higher signal in the RE band than the NIR band. Both bands were increasingly absorbed by water as depth

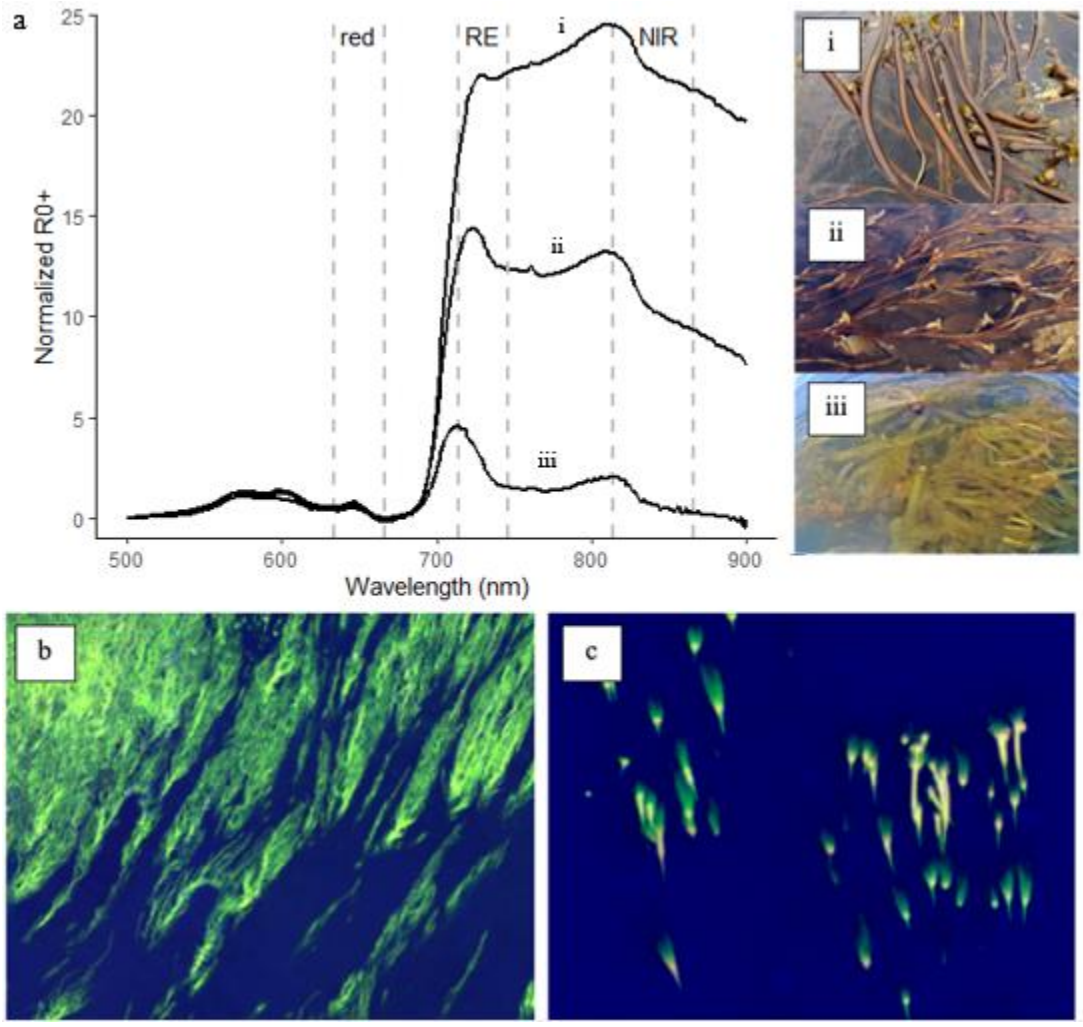

Figure 10. *In situ* spectral information and accompanying photos for (i) dense *Nereocystis* pneumatocysts (ii) dense *Macrocystis* fronds, and (iii) dense *Nereocystis* blades. For each spectrum, the accompanying photo was taken as the spectrum was collected. Spectral plots have overlayed red, red-edge (RE), and near-infrared (NIR) bandwidths of the DJI Phantom 4 multispectral sensor, which was used to create false colour RGB images of b) *Macrocystis* and c) *Nereocystis*. For both UAV images, the NIR band was assigned the red channel, the RE band was assigned the green channel, and the red band was assigned the blue channel. Therefore, if a pixel of kelp canopy had a higher value in the NIR band than the RE band, the pixel appeared more orange/red; if the pixel had a higher value in the RE band than the NIR band, the pixel appeared greener, and if the two bands were roughly equal the pixel appeared yellow.

increased and appeared darker towards the distal ends of the blades. The denser patches of *Macrocystis* canopy in the center of the bed were most buoyant and appeared bright yellow, indicating a similar magnitude of the signal in the NIR and RE bands (Figure 11b). However, the majority of the *Macrocystis* canopy was green, indicating submersion below the water surface and a higher signal in the RE band versus the NIR band, with the signal from both bands being absorbed by water around the frond edges.

The optical constituents and optical characteristics of the water between sites and days showed a very small range of variability (Table 7). The range of TSM concentration remained relatively low (2.8-3.8 mg/l) spatially (among sites) and temporally (between days), with conditions representing low concentrations for summer coastal waters in BC (Phillips and Costa, 2017). PIM (58.8 $\pm$ 4.22%) was slightly higher than POM (41.2 $\pm$ 4.22%) at each site, but neither was dominant in the system over the survey period, representing a combination of inorganic and organic particulates. The low range of TSM agreed with the low variability seen in Secchi depths for the same sites and days (4.1 $\pm$ 1.07 m), further indicating that turbidity levels in the water were similar during surveys.

Table 7. Water optical properties and parameters for each site and averages over the survey period. TSM = total suspended matter; POM = percent organic matter; PIM = percent inorganic matter; K_d = diffuse attenuation coefficient; R_{0+} = above water reflectance. Site codes are in Table 3.

Site	SP	WB	TA	WM	TQ	SF	Mean ± sd
Date (2020-DD-MM)	03-07	04-07	05-07	06-07	07-07	09-07	-
Secchi (m)	4.5	3.0	3.5	3.5	4.0	6.0	4.1 ± 1.07
TSM (mg/L)	3.8	3.5	3.1	3.4	3.4	2.8	3.3 ± 0.34
POM (%)	35.8	39.4	44.5	45.1	45.2	37.4	41.2 ± 4.22
PIM (%)	64.2	60.6	55.5	54.9	54.8	62.6	58.8 ± 4.22
K_d (650 nm)	0.57	-	0.54	0.34	0.52	0.21	0.43 ± 0.16
K_d (715 nm)	1.10	-	1.09	0.72	1.10	0.93	0.98 ± 0.17
K_d (788 nm)	1.59	-	1.84	1.25	1.61	1.49	1.56 ± 0.21
R_{0+} (650nm)	-	0.75	0.48	0.44	0.46	0.53	0.53 ± 0.13
R_{0+} (715nm)	-	0.38	0.25	0.25	0.19	0.24	0.26 ± 0.07
R_{0+} (788 nm)	-	0.14	0.15	0.07	0.10	0.05	0.10 ± 0.04
R_{0+} (840 nm)		0.10	0.04	0.01	0.05	0.02	0.04 ± 0.04

Evidence of the low spatial and temporal variability of the optical water constituents and Secchi depths were also supported by the normalized deep-water spectra (Figure 12a). These spectra showed that the spectral characteristics of water were most variable in the blue and green wavelengths. The spectral features of water were highly similar between sites at red (~650 nm), RE (~715 nm), and NIR (~840) wavelengths, showing relatively low R_{0+} and minor differences in R_{0+} between sites (0.31%, 0.19%, and 0.09% respectively). All deep-water spectra showed a strong peak at 570 nm and a small fluorescence peak at ~690 nm, yet none of the spectra had peaks in the RE or NIR that would have indicated high water turbidity due to a phytoplankton bloom or high concentrations of inorganic particulates (Kutser, 2009; Phillips & Costa, 2017). The K_d data (Figure 12b) supported the above water hyperspectral data for all sites, with the lowest average K_d values corresponding to the strong R_{0+} peaks at 570 nm in the above-water

spectra and increasing as the R_{0+} decreased at longer wavelengths. Above ~700nm, the K_d were highly variable compared to the K_d at visible wavelengths, likely associated with signal-to-noise issues due to the high attenuation at these long wavelengths (Pegau *et al.*, 1997). Regardless, average K_d in the NIR (788 nm) was roughly 1.5 times that of the average K_d in the RE (715 nm) and average K_d in the RE was twice that of average K_d in the red (650 nm). As expected, these K_d values indicate that attenuation of light in the water column generally increases at longer wavelengths of the electromagnetic spectrum.

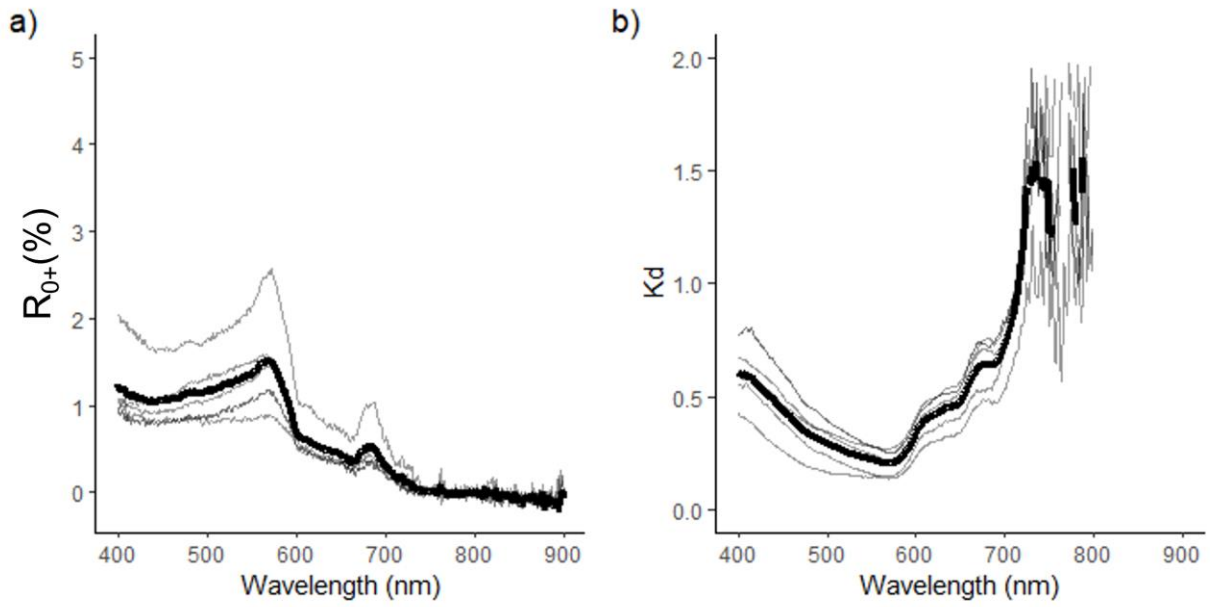

Figure 11. Summary of a) the percentage of light reflectance (R_{0+}) between 400-900 nm from deep-water spectra during surveys; and b) Diffuse attenuation coefficient (K_d) between 400-800 nm for the top meter of the water column during surveys. For each, the thick black line indicated the mean values over the survey period and the grey lines show the variability of measurements between days.

Together, the *in situ* spectral information for kelp and water showed high variability in the RE and NIR wavelengths for kelp due to varying levels of submergence for different structures, and low variability in the spectral characteristics of water due to similar optical properties between

survey days. Therefore, comparisons between the NDRE and NDVI classified UAV imagery can inform on the overall differences in kelp surface canopy detection when using either index for classification. However, this information should be considered with the pretext that water optical conditions seen here may differ in other regions or at different times of year.

Pairwise comparisons between surface-canopy areas classified from NDRE and NDVI in UAV imagery determined that more kelp was detected using the NDRE index ($t = 7.17$, $df = 58$, p-value < 0.001). For all surveys, the summed total of kelp area classified with NDRE area was 1.18 times higher than kelp area classified with NDVI. The larger area of kelp detected with NDRE did not change between *Macrocystis* and *Nereocystis* beds ($t = -0.07$, $df = 51$, p-value = 0.95), nor did it differ significantly based on tidal height ($t = -0.54$, $df = 27.7$, p-value = 0.59).

3.4.2 Tide and Current Relationships

The multispectral UAV data used to map kelp bed extent were analyzed alongside *in situ* tide and current data to characterize the influence of tide and current on surface canopy area. ADCP data showed that UAV flights for all sites took place while current speeds were less than 10.0 cm/s (Figure 13). The exception was seen for surveys conducted at the Triquetta where current speeds of up to 19.0 cm/s were recorded during imagery collection. Further, although *Macrocystis* beds were not subject to high-current speeds during UAV imagery acquisition, the ADCP was running continuously during the survey days, and detected high current speeds similar to those detected at Triquetta and the Westbeach *Macrocystis* bed during high tide (21cm/s @ 3.8 m) and at the Surf Pass mixed bed during low tide (13 cm/s @ 0.5 m), indicating that brief high-currents speeds may occur at any tidal height regardless of species. These data points were not included in the analyses of the tide-current-area relationships since they were not recorded during imagery collection.

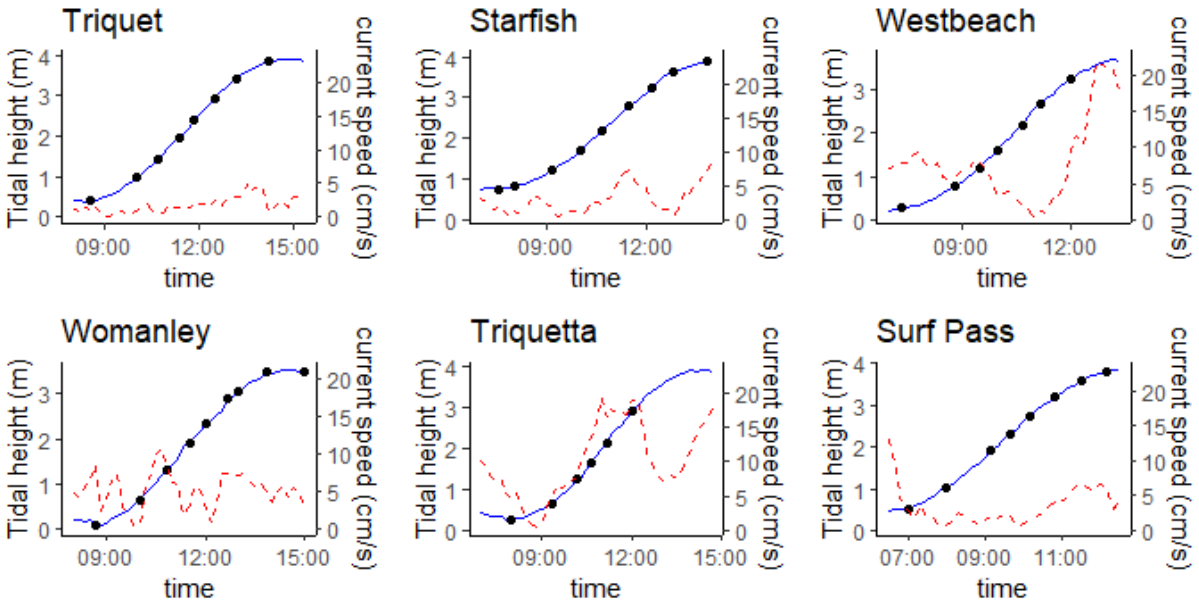

Figure 12. Plots for each site showing current speed (red dashed line) and tidal height (blue line). UAV flights (black dots) that resulted in successful orthomosaics are shown overlayed at their respective tidal heights (m) on the blue line.

Multiple regression models showed that the combination of tide and current explained between 91-96% of the variability seen in the surface-canopy areas of kelp over a tidal cycle (Table 8). For six out of eight kelp beds, tidal height had a negative effect ($p < 0.05$) but current had no effect ($p > 0.05$) on surface-canopy area. Despite having high adjusted-R^2 values, two out of eight beds (both at Triquetta) showed no significant effects ($p > 0.05$) for either independent variable. For these beds, high VIF values (VIF>10 ; Faraway, 2002) indicated that tidal height and current speed were highly correlated (collinearity), meaning that support for the coefficient estimates was weak, and either tidal height or current speed should be removed from the model to improve support for the coefficient estimates (Faraway, 2002).

Table 8. Results of Multiple regression coefficients (+/- standard error) with variance inflation factors (VIF) for the independent variables. ***<0.001, **<0.01 *<0.05. Bed codes are defined in Table 3.

Bed code	Tidal height	Current speed	VIF	Adj. R^2
TQ	-342.3±44.9***	-136.5±3961.3	1.3	0.91
SF_N	-152.6±12.6***	-355.1±596.8	1.3	0.96
SF_M	-136.9±13.6***	-509.6±647.3	1.3	0.94
WB	-581.8±72.6**	-4067.7±2405.9	1.1	0.91
WM	-1711.0±157.4***	5431.7±7400.9	1.0	0.94
TA_1	-455.1±436.1	-6820.5±6735.3	24.3	0.95
TA_2	-109.9±37.1	375.6±561.9	14.5	0.95
SP	-157.9±40.3*	654.7±1613.2	5.8	0.92

After removing current speed as an independent variable, simple linear regression models between surface-canopy area and tidal height showed strong negative linear relationships for all eight kelp beds surveyed (Figure 13). Here, tidal height alone explained roughly the same level of variability in surface-canopy ($R^2 > 0.9$ for all sites) area as the combination of tidal height and current speed in multiple regression models. The surface-canopy area of the Triquetta beds decreased at nearly twice the rate of the beds at the other sites ($t = -5.54$, $df = 6$, p-value = 0.001), suggesting that current speeds above 10cm/s influence surface-canopy area alongside the normal effects of tidal height while detected surface canopy area at sites with current speeds below 10cm/s are mainly affected by tidal height. Due to the large range in current speeds at *Nereocystis* beds, the rate of decrease for surface-canopy area ranged nearly three times greater for *Nereocystis* beds than for *Macrocystis* beds (Table 9, Figure 13).

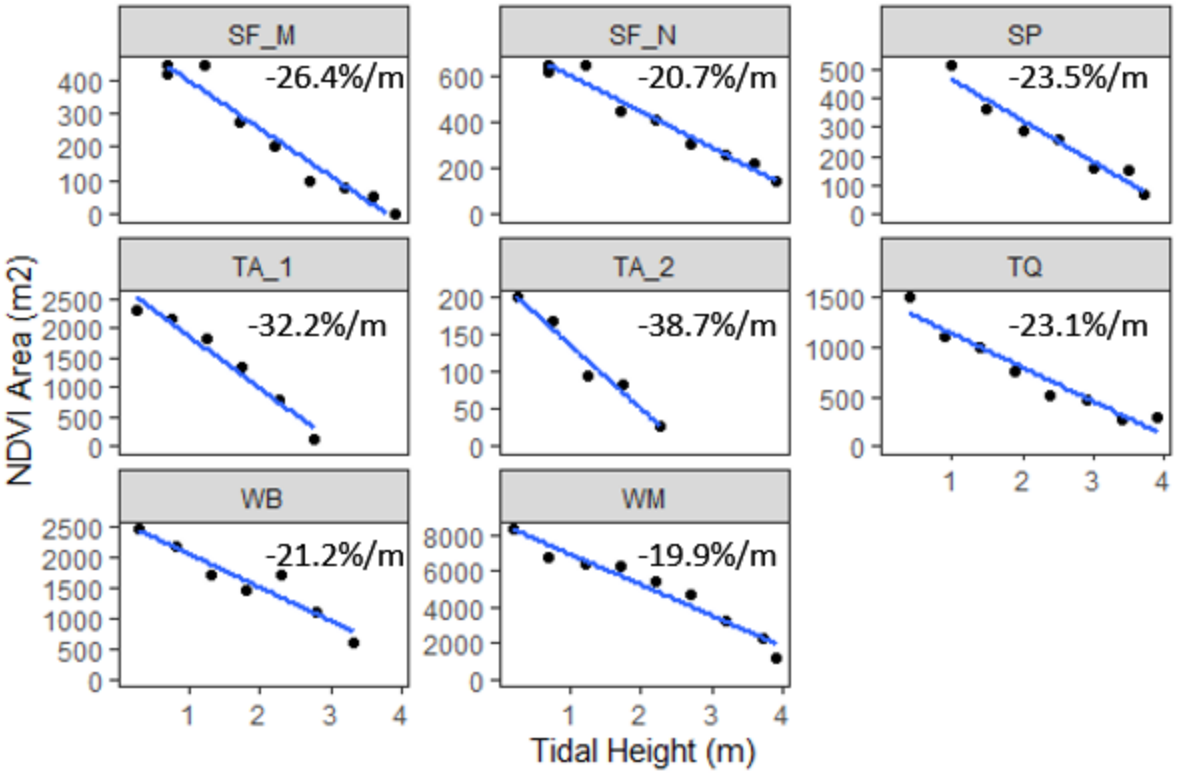

Figure 13. Plots showing the linear relationship between the NDVI classified surface-canopy area and tidal height for the sampled beds, including the percentage of decrease in surface-canopy area per meter of tidal height increase (i.e., slope). Bed codes are defined in Table 3.

Table 9. Descriptive statistics of kelp bed characteristics when grouped by both species and current using NDVI for classification.

Grouping	# of beds	Mean ± sd area decrease (%/m)	Range of area decrease (%/m)	Range of current speeds (cm/s)
All beds	8	-25.7 ± 6.6	-19.9 to -38.7	0.0 to 19.0
Nereocystis	3	-30.5 ± 9.1	-20.7 to -38.7	0.0 to 19.0
Macrocystis	4	-22.7 ± 2.8	-19.9 to -26.4	0.0 to 9.6
Mixed spp.	1	----	-23.5	0.7 to 7.1
Low-current	6	-22.5 ± 2.4	-19.9 to -26.4	0.0 to 9.6
High-current	2	-35.5 ± 4.6	-32.2 to -38.7	4.6 to 19.0

Despite the fact that the surface canopy area of beds classified with NDRE decreased at a slightly lower average rate (mean ± sd: -24.3 ± 5.3%/m) than the surface canopy classified with NDVI (-25.7 ± 6.6%/m), there was no statistical difference in the rate of decrease between either NDVI or NDRE classified data ($t = 0.49$, $df = 14$, p-value = 0.635). However, since using NDRE detected a larger area of kelp area than NDVI (section 3.4.1), the average area of kelp detected by NDRE was always greater at any given tidal height than NDVI (Figure 14). For example, with *Macrocystis* beds, both NDVI and NDRE values were higher at the center of the kelp bed, and lower towards the bed edge. Yet the higher RE signal from submerged kelp at the edges allowed some pixels with negative average NDVI values to have positive average NDRE values. This means that while NDVI and NDRE will positively classify dense kelp at the center of a bed, using NDRE will positively classify more kelp at the bed edges than NDVI.

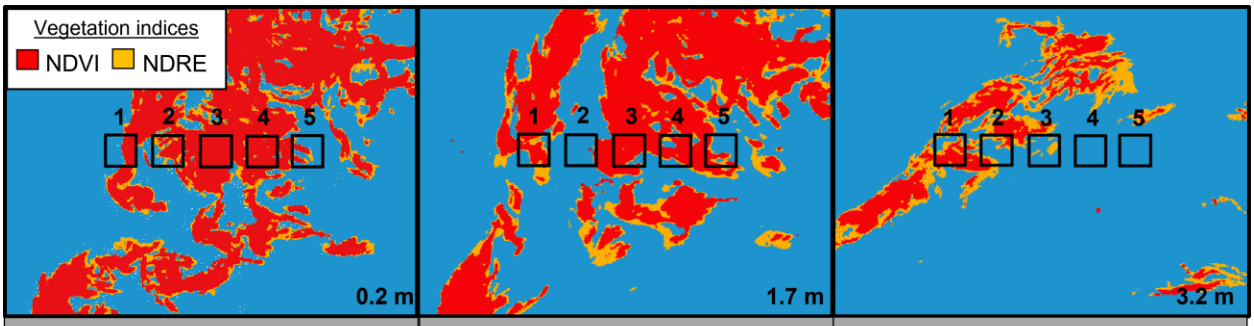

0.2 m Area	NDVI (mean ± sd)	NDRE (mean ± sd)	1.7 m Area	NDVI (mean ± sd)	NDRE (mean ± sd)	3.2 m Area	NDVI (mean ± sd)	NDRE (mean ± sd)
1	0.13 ± 0.29	0.22 ± 0.32	1	0.10 ± 0.31	0.37 ± 0.30	1	0.10 ± 0.16	0.28 ± 0.16
2	0.13 + 0.19	0.31 ± 0.19	2	-0.29 ± 0.19	-0.16 ± 0.20	2	0.00 ± 0.13	0.18 ± 0.15
3	0.51 ± 0.15	0.60 ± 0.13	3	0.45 ± 0.32	0.60 ± 0.26	3	-0.10 ± 0.04	0.08 ± 0.09
4	0.41 ± 0.15	0.54 ± 0.12	4	0.22 ± 0.35	0.44 ± 0.31	4	-0.14 ± 0.02	-0.05 ± 0.02
5	-0.08 ± 0.22	0.05 ± 0.25	5	-0.08 ± 0.36	0.13 ± 0.38	5	-0.15 ± 0.02	-0.06 ± 0.02

Figure 14. NDRE (orange) and overlayed NDVI (red) classified Macrocystis from orthomosaics at tidal heights of 0.2, 1.7, and 3.2 meters. Five 2 m x 2 m pixels overlay each orthomosaic at the same coordinates, and the NDVI and NDRE values (mean ± sd) for each pixel are listed below.

3.5 Discussion

Overall, field observations paired with hyperspectral data showed that *in situ* spectral differences in the RE and NIR regions of different structure types were observed as a result of variable buoyancy amongst surface canopy structures. In addition, multispectral UAV data showed that at the bed scale, spatially, there were similar magnitudes of RE and NIR reflectance for both species of kelp, with RE generally higher near the bed periphery where kelp structures were often submerged, and NIR higher than or equal to RE near the bed centers where the surface-floating kelp was most dense. This difference led to an 18% increase in classified aerial kelp extent using NDRE as the classification input compared to using NDVI. The classified aerial extents were strongly negatively impacted by tidal height (average of -25.7 $\pm$ 6.6% decrease per meter increase in tidal height), and most were not impacted by currents, however, this was likely a result of the low relative currents (<10cm/s) measured at most study areas. The spectral characterization of kelp structures and water, as well as the effects of tides and currents can be compared with other studies to provide generalized recommendations for the application of kelp remote sensing.

3.5.1 Spectral Characterization of Kelp Canopy and Water at the kelp structure and bed scales

Choosing appropriate spectral bands is a key consideration for the classification of specific targets in remote sensing imagery, and to ensure that appropiate bands are selected requires an understanding of the spectral charactersitics of the different classes of interest within an image. Specifically for kelp mapping, the aim is to choose spectral bands that maximise the separability between the surface-canopy of two classes, kelp and water (Jensen, 1980; Schroeder *et al.*, 2019b). Therefore, it is important to understand how the specific morphologies of different kelp canopy structures relate to the varying levels of buoyancy, and ultimately, emergence at the

water's surface, because submerged kelp canopy can have a substantially lower reflectance signal in the RE and NIR regions and reduced spectral separability with water.

Additionally, it is important to consider that water optical constituents can be highly variable both spatially and temporally, potentially attenuating light in the water and causing variability in above-water reflectance measurements of the submerged kelp. The concentrations of water optical conditions were very similar during our surveys, and therefore the measured kelp reflectance from the *in situ* hyperspectral data and UAV imagery was primarily attributed to variability within and between kelp beds rather than changes in the water. For example, the above-water spectra for all sites were marked by low reflectance in the red wavelengths and a small fluorescence peak at ~690 nm, which indicated the presence of phytoplankton (Sathyendranath *et al.*, 1987; Roesler & Perry, 1995; Phillips & Costa, 2017), yet POM levels indicated that organic matter was not dominant in the system and none of the above-water spectra showed peaks in the RE or NIR that would have indicated an especially strong phytoplankton bloom (Kutser, 2009). In addition, the low R_{0+} at the red wavelengths and the low TSM concentrations [2.8-3.8 mg/l] indicated that the surveyed areas also had a low sediment load compared to BC regions with high estuarine influence (Phillips & Costa, 2017). During all surveys, the lowest measured K_d was at ~570 nm and increased continuously at longer wavelengths, giving further evidence supporting the homogenous water properties among sites and days.

Although the bio-optical properties observed during this study had low spatial and temporal variability, generally, these properties can be highly variable both spatially and temporally on the coast of British Columbia (Loos & Costa, 2010; Phillips & Costa, 2017; Giannini *et al.*, 2021). Undocumented changes in water optical properties may bias classification results by obscuring

spectral features used to detect aquatic vegetation (Dekker *et al.*, 2005; O'Neill & Costa, 2013). Specifically, intense phytoplankton blooms can increase reflectance in the NIR region of the spectra, especially at the RE wavelengths (Schalles *et al.*, 1998). In addition, glacial fjords and estuaries are common along the coast of British Columbia, characterized by high sediment loads, which greatly increase the reflectance across all wavelengths between the red and the NIR in water spectra (Ritchie *et al.*, 2003; Phillips & Costa, 2017), thereby reducing the ability to detect submerged targets (Dekker *et al.*, 2005; Murray *et al.*, 2015). Therefore, although there was low variability in water optical conditions during our surveys, these parameters should not be ignored when considering spectral bands to use for kelp mapping.

Kelp surface canopy is often considered a single class in remote sensing imagery (Nijland *et al.*, 2019; Schroeder *et al.*, 2019a; Bell *et al.*, 2020), yet for different kelp structures, the relative magnitudes of NIR to RE varied according to the amount of emergent kelp at the water surface (Figure 11a). Reflectance at the RE peak for submerged structures was higher relative to the NIR peak, which was combined result of the reflectance from the submerged kelp and the attenuation by water and its optical consituents. Generally, when kelp is emergent above the water surface, the NIR signal is higher than the RE signal regardless of structure type (e.g. see section 2.4.1). Yet, when kelp canopy is submerged, our K_d measurements showed that the NIR signal was attenuated at nearly 1.5 times the rate of the RE signal (Figure 15), resulting in a higher overall above-water reflectance in the RE than the NIR.

The relative strength of the signal at the RE and NIR wavelengths can help inform whether kelp canopy in remote sensing imagery is submerged. However, common methods for satellite imagery kelp mapping make use of $VI_{n,}$ (equation 2), which beyond RE and NIR, also considers a visible wavelength (Tucker, 1979; Schroeder *et al.*, 2019a). In these cases, it is important to

consider the the magnitude of the reflectance signal in band 2 (e.g., RE and NIR) relative to the signal in band 1 (here, the red band; Equation 4). For instance, as kelp is submerged, the reflectance in band 2 decreases faster than in band 1, and if the signal of band 2 is lower than band 1 the VI_n value becomes negative and will likely fall below the general defined detection threshold (Nijland *et al.*, 2019; Mora-Soto *et al.*, 2020). Here, for VI_n considering either the NDVI or NDRE based on multispectral bandwidths simulated from our hyperspectral data, the outputs are positive regardless of kelp structures. Therefore, despite the differences in reflectance between kelp structures at or very near the surface, all structure types for our dense samples could be positively classified with either NDRE or NDVI. However, the ability to detect deeper submerged kelp canopy will vary based on the R_{0+} magnitude of each kelp structure, the bio-optical properties of the water, and the depth at which the structure is submerged. Overall, the RE wavelengths are absorbed less by water, and therefore choosing RE over NIR wavelengths to classify kelp in remote sensing imagery will increase the amount of the submerged kelp canopy that is detected.

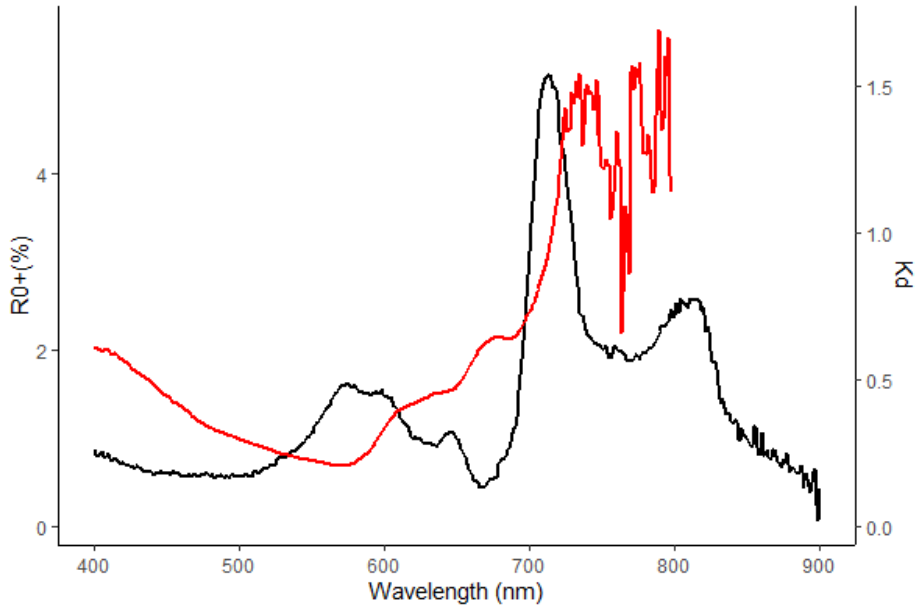

Figure 15. Above-water spectra of submerged *Nereocystis* blades (black line) showing the red edge peak (~710 nm) at slightly shorter wavelengths than the exponential increase in K_d (red line), resulting in more than twice the reflectance (R_{0+}) compared to the near infrared peak (~820 nm).

In addition to understanding the effects of submergence on the spectra of individual surface-canopy structures in combination with the optical properties of the water, it is also important to understand how the submergence of kelp canopy affects the above-water detection of kelp within different regions of the kelp bed. The multispectral UAV imagery showed that for both species the strength of the RE or NIR signal varied according to the presence and density of the different structure types. In general, pixels corresponding to kelp canopy showed the highest signal in the NIR and RE bands towards the center of the beds, with NIR often being slightly higher than RE, as seen in the emergent kelp canopy. Both NIR and RE signal were lower at the bed periphery, yet here, the RE signal generally remained much higher than the NIR. As a result, about 18% more kelp canopy area was detected across all orthomosaics when using NDRE instead of NDVI for *Macrocystis* and *Nereocystis*. This effect is demonstrated in Figure 14, where the NDRE classified kelp can be seen extending beyond the edges of the NDVI classified kelp at low, medium, and high tidal heights.

For *Macrocystis* specifically, the higher area detected with NDRE is likely explained by a combination of varying kelp density and the strength of local currents in different areas of the beds. For instance, the high spatial resolution UAV imagery (~5cm) showed that frond density in *Macrocystis* beds was generally highest towards the center of the bed compared to the periphery (Figure 11b) where the fronds were sparser. Therefore, in imagery with lower spatial resolution (e.g. 30m for Landsat), pixels at the bed periphery are more likely to contain a mix of kelp and water endmembers (Bell *et al.*, 2020). The UAV imagery also showed that pixels containing 100% frond near the bed periphery had a lower overall signal at the NIR band than pixels

containing 100% frond near the center of the bed. Also, these peripheral pixels generally had higher signal at the RE band relative to the NIR band. Taken together with field observations, these data indicate that peripheral *Macrocystis* fronds are likely to have lower above-water reflectance because they are generally more submerged compared with fronds at the bed center. It is possible that the peripheral fronds are simply less buoyant (i.e. either smaller or fewer pneumatocysts on the fronds), but at the periphery, fronds are also exposed to higher current speeds compared to the centre of the bed (Valle-Levinson *et al.*, 2022), likely causing more submersion.

Similarly, for *Nereocystis*, additional canopy was detected at the bed periphery when NDRE classification was used rather than NDVI. Field observations showed that the pneumatocysts peripheral *Nereocystis* were commonly submerged, and the majority of additional canopy area detected was blades that were held horizontal just below the water surface. In contrast, both field and UAV imagery observations also revealed that there was a higher density of emergent pneumatocysts towards the center of the beds where the blades often hung slack in the water column and were not detectable regardless of the index used for classification. Thus, although *Macrocystis* and *Nereocystis* have morphologically distinct canopy structures, both species had a higher areal extent detected using RE indices with the majority of extra canopy being submerged structures detected near the bed periphery.

3.5.2 Tide and Current Analysis

Kelp morphological and environmental factors are interconnected and should be considered when analyzing remotely sensed imagery for kelp mapping. However, these factors may also vary spatially and temporally. For example, environmental factors such as availability of light and nutrients, or exposure to local currents can cause kelp surface-canopies to vary

morphologically within species (i.e. phenotypic plasticity) (Druehl & Wheeler, 1986; Coleman & Martone, 2020), resulting in both inter- and intra-specific differences in the density and buoyancy of surface-canopy for kelps that occupy different habitats and regions (Druehl, 1978; Mora-Soto *et al.*, 2020; Cavanaugh *et al.*, 2021b). As such, for the purposes of imagery analysis, it is important to define the effects of tidal height and current speed on surface canopy area, not only between species, but also within the same species found in different oceanographic regions with varying tidal regimes (Schroeder *et al.*, 2019b; Cavanaugh *et al.*, 2021a). Although our study provides knowledge applicable to global mapping of surface-canopy forming kelp, results are cautiously considered in the context of other studies with similar tide and current regimes, but considering different temporal, spatial, and spectral resolutions.

The classified area of *Nereocystis* beds decreased with tidal height at a higher and more variable rate (-30.5 $\pm$ 9.1 %/m), than both *Macrocystis* beds (-22.7 $\pm$ 2.8 %/m) and the mixed bed (-23.5 %/m). The difference between the *Nereocystis* and *Macrocystis*/mixed beds is hypothesized to be a result of the wide range of current speeds during UAV flights at the *Nereocystis* sites (0.0 - 19.0 cm/s) versus the narrower range measured at *Macrocystis sites* (0.0 - 9.6 cm/s) and the mixed site (0.7 - 7.1 cm/s). However, when currents speeds were low (<10 cm/s), the surface-canopy areas decreased at a similar rate (-22.5 $\pm$ 2.4 %/m) for all sites regardless of species. In these low current conditions, despite the distinct morphologies of *Macrocystis* and *Nereocystis*, the buoyant forces that result from the pneumatocysts and fronds hold the kelp canopy of each species at the water surface. As the tidal height increases, the basal ends of the floating portion of the surface-canopy (*Macrocystis* frond or *Nereocystis* pneumatocyst) are pulled below the surface of the water at roughly the same rate. This process takes place for each sporophyte within

the kelp bed simultaneously, and as a result, tidal height alone explained more than 90% of the variability in surface-canopy area over the tidal cycle at low-current sites.

For high current conditions, the data analysis is limited to *Nereocystis* because the only site with high current speeds (Triquetta; 4.6 - 19.6 cm/s) contained two separate *Nereocystis* beds. Here, the average rate of decrease (-35.5 $\pm$ 4.6 %/m) was nearly twice that of the sites with lower current speeds (-22.5 $\pm$ 2.3 %/m) (Table 9). We hypothesize that for these high current conditions the submergence of the basal portion of the canopy with increased tide happens at the same rate as it would at in low current conditions, however, the high current adds horizontal drag to the sporophyte stipe, pushing it diagonally in the water column, resulting in further submersion of the basal portion of the surface canopy. Therefore, as the tide rises and current speeds increase concurrently, the apparent area of surface-canopy decreases at a faster rate than at low current speed conditions.

The high rate of change for high current conditions is similar to the trends reported by Britton-Simmons *et al*. (2008). This study, in the Strait of Juan de Fuca, Washington, had current conditions that were much higher (>100cm/s). These extreme current speeds decreased the extent of kelp canopy between 50% to nearly 100% over a one-meter increase in tidal height. Similar to our results, they showed that currents below 10 cm/s had no effect on surface-canopy area. Their study, however, used oblique angle colour-photography from land-based vantage points which may have resulted in an overestimation of the effect of the currents (Britton-Simmons *et al*. 2008).

At *Macrocystis* beds, the measured current speeds were generally lower (0.0-9.6 cm/s) than at *Nereocystis* beds, which is typical for this species as it grows in less hydrodynamically active environments (Springer *et al.*, 2007). However, there was one period at Westbeach, where the

ADCP collected data outside the analyzed imagery (3.8m tidal height). This data revealed that *Macrocystis* beds in low current areas can also be subject to brief, periodic increases in currents (~21.0 cm/s) with potential to suddenly submerge large portions of the canopy. Unfortunately, this portion of the dataset was not part of the UAV analysis because Metashape was unable to stitch the UAV imagery from the concurrent flight into an orthomosaic due to a lack of valid tie-points (section 3.3.2). Therefore, although *Macrocystis* may also be periodically submerged by high current speeds, more investigation is needed to understand the strength of this effect.

During low current conditions (<10cm/s), over 90% of the variability in the negative linear relationships between tides and *Macrocystis* canopy extent was explained by tidal height alone. The high explanatory power of tidal height in these relationships was similar to that reported for the same species in low current (< 13cm/s) areas of California (Cavanaugh *et al.* 2021b). However, in our study the slopes of these relationships were all highly similar (-19.9 to -26.4%/m) while the slopes differed across the two California sites. Cavanaugh *et al.* (2021b) suggested that these differences were due to differences in the morphology of the two beds examined, i.e., kelp growth in deeper waters resulted in longer fronds and denser canopies relative to shallow waters. Specifically, based on the two *Macrocystis* beds assessed, a sparse bed in shallow waters (max. depth 8 m) and a dense bed in deeper waters (max. depth 16 m), the dense bed decreased at half the rate (-12.7%/m) of the sparse bed (-20.1%/m). The estimated rate was based on our interpretation of Cavanaugh *et al.* (2021b) but using the lowest tidal height (-0.55 m MLLW) as a benchmark to estimate maximum kelp at the surface (as described in section 3.3.3). Therefore, sparse kelp beds in shallow waters in California had a similar relationship with tidal height as the *Macrocystis* beds in our study (-22.7%/m) within similar depth conditions (max. 5 m deep). Note that we have no metrics to directly compare the density between the

California beds and those in our study, and it is important to note that both California beds were 2-3 times larger than the largest bed we surveyed (Figure 13) and the sparse bed had a larger areal extent than the dense bed, indicating that bed size alone did not impact the rate of mapped bed decrease. Nonetheless, the mechanism is unclear for how the morphology (i.e., length of fronds or density) of kelp beds might affect the rate of surface canopy submersion under similar tidal conditions when current was not a factor, and it is unclear if similar relationships may be found on the coast of British Columbia.

3.5.3 Implications for satellite remote sensing of kelp areal extent using different spatial and temporal resolutions

Our results describe the effects of tidal height and current speed on the area of kelp surface-canopy detected by a very high spatial resolution (~5cm) multispectral sensor at high temporal resolution (up to 9 times over a single tidal cycle). However, kelp forest mapping is often conducted using satellite imagery on a regional scale using either high spatial resolution (< 5m) or medium spatial resolution (10-30 m) imagery, generally acquired at a lower temporal resolution (acquisition weeks or months apart). Therefore, the results should be considered in light of the spatial and temporal artifacts typical of satellite imagery collection and analysis, including multi-year time series with satellite imagery using a single image acquired during peak kelp growth at the low range of tidal heights (Schroeder *et al.*, 2019a) or aggregate results of all imagery acquired over a period of time (Cavanaugh *et al.*, 2011; Nijland *et al.*, 2019; Bell *et al.*, 2020). In either scenario, the relationships provided by this study can be applied to evaluate uncertainties associated with tidal height in the derived kelp surface area. For example, Schroeder et al., (2019b) and Hamilton et al. (2020) used a maximum acceptable tidal height of ~2 m (LLWLT) as a tidal threshold for *Nereocystis* detection with satellite imagery. Our results suggest that with these tidal conditions, differences in kelp extent between 45-61% should be

expected from images collected between 0m and 2m tidal height. Specifically, Schroeder *et al.* (2019b) examined fringing kelp along narrow channels with high current speeds. In such cases, it may be beneficial to compare multiple images within the same year, or analyze both NIR and RE classifications to reduce the chance of underestimating the area of kelp due to submergence (Finger *et al.*, 2021). If a large amount of imagery is available for the region of interest, selecting narrower tidal windows will also allow the user to reduce uncertainties related to tidal heights, with lower tidal heights producing the most kelp canopy at the surface. On the Oregon coast, Hamilton *et al.* (2020) examined large, offshore *Nereocystis* beds with offshore currents between 5-10cm/s on average, and highs of around 15cm/s (Wyatt *et al.*, 1972). However, nearshore currents can be completely decoupled from general oceanographic trends (Britton-Simmons *et al.*, 2008) and therefore it should not be ruled out that some of the extreme variability (larger than the expected 45-61%) seen between individual years by the authors may have been due in part to local surface currents submerging large portions of the Nereocystis canopy during imagery acquisition.

The spatial resolution of the satellite imagery and the classification methods used may also play an important role in kelp detection under various tide/current scenarios. Nijland *et al.* (2019) acquired paired imagery of the same area at two different tidal heights with both WorldView-2 (2 m spatial resolution; 1.5 and 3.6 m tidal height) and Landsat-8 (30 m spatial resolution; 0.6 and 2.7 m tidal height), each roughly one month apart over an exposed group of islets (the McMullin island group) just north of the kelp beds surveyed in this research, where large, dense, and contiguous *Macrocystis* beds occur at shallow depths (< 5m). Based on their results, standardized to a 0m tidal height (LLWLT) as a benchmark for maximum kelp area, we estimated a kelp area decrease of -18%/m with WorldView-2 and -15%/m with Landsat-8 with

increased tide; this is lower than the average decrease for low current sites in our higher spatial and temporal resolution study (-22.5 %/m). One potential explanation is that the exceptionally dense McMullin beds decreased at a lower rate than sparse beds, as was documented in the large dense bed surveyed by Cavanaugh et al., (2021b). However, it is also possible that the reduced rate of decrease is simply an artifact of the lower spatial resolution and the thresholding methods used by Nijland *et al* (2019). For example, in the adopted methods, a pixel of Landsat imagery must only contain around 20% of the reflectance signal of surface-canopy to be positively classified as a kelp (Hamilton *et al.*, 2020; Bell *et al.*, 2020). As such, our data suggest that with a decrease of 22.5%/m, a pixel containing 100% kelp canopy at 0 m could be submerged up to 3.5 m tidal height and still be positively classified with a binary threshold in Nijland *et al*.'s (2019) Landsat pixel. Therefore, as the spatial resolution of imagery decreases, the use of a binary threshold to classify large contiguous kelp beds may over-estimate surface-canopy area at higher tidal stages. If so, the estimation of kelp fraction per pixel (i.e., MESMA) will likely give more accurate estimates for kelp surface-canopy area across different tidal heights (Cavanaugh *et al.*, 2011).

Finally, derived kelp surface-canopy may vary substantially when using the RE and NIR wavelengths depending on both the type of kelp structure(s), submergence, and whether the pixel is near the center or periphery of the bed. These differences were visually distinguished in the very high spatial resolution imagery of our study but are much harder to parse apart in high or medium (<5 – 30 m) satellite imagery. For example, a pixel that contains an extent of 100% *Nereocystis* pneumatocysts generally has a higher reflectance signal than a pixel that contains the same percentage of *Macrocystis* fronds or *Nereocystis* blades. Therefore, if a *Nereocystis* pneumatocyst is used as an end-member for determining the fraction of *Macrocystis* fronds or

Nereocystis blades within a pixel, the kelp fraction for that pixel will be underestimated. Additionally, our results suggest that if MESMA is being used to estimate kelp biomass within satellite resolution imagery (Cavanaugh *et al.*, 2011), incorporating the RE band may allow for increasingly accurate biomass estimation by detecting more of the submerged portions of surface-canopy. Yet despite the potential to use RE wavelengths to detect more submerged kelp canopy, classifying nearshore kelp on a satellite imagery requires additional attention when imagery is acquired at low tides. For example, nearshore *Macrocystis* and *Nereocystis* kelp forests often contain various species of understory vegetation, such as *Pterygophora california* which forms a secondary benthic-canopy up to two meters off the sea floor (Shaffer, 2000; Druehl & Clarkston, 2016). Therefore, the use of RE bands for kelp area mapping over nearshore areas during the lowest tides may result in errors of comission, where benthic-canopy species are erroneously classified as kelp canopy. Specific to our study sites, subtidal *Pterygophora* beds were mixed with shallow *Macrocystis* beds at two separate sites. At 0.5 m tidal height, the *Pterygophora* canopy was detectable in UAV imagery with both NDRE and NDVI classification, yet by 1.0 m tidal height the *Pterygophora* canopy was only detectable with the NDRE. Given this source of error, these locations were noted and avoided in the analyses, yet satellite imagery users with no access to field observations may misclassify this type of data as kelp canopy. While MESMA allows the user to determine the kelp and water fractions within a pixel, the spectral signatures of understory and surface-canopy kelps are highly similar, making it difficult to differentiate when both types are at or near the surface. Therefore, if one wishes to avoid overestimation of surface-canopy area due to misclassification of understory canopy, caution should be exercised when monitoring nearshore kelp beds at the lowest tides, especially with RE indices, and using NIR based indices like NDVI may help reduce these potential errors.

3.6 Conclusion

Submergence of kelp canopy is associated with physical drivers, including tides and currents, and buoyancy differences between surface-canopy structures. In this study, *in situ* hyperspectral samples were used to characterize the differences between *Nereocystis* and *Macrocystis* surface-canopy structures. Multispectral UAV imagery was used to investigate spatial differences in these characteristics at the bed level, as well as the relationship between the surface-canopy areas of both *Nereocystis* and *Macrocystis* with tidal height and current speed. Our results can be used to interpret trends collected across a range of tidal heights and currents, by providing general 'correcting factors' for these differences and providing site-specific metrics of potential variability in bed extent. Tidal height had a strong negative linear relationship with the surface-canopy area of both *Macrocystis* and *Nereocystis* at all sites. In low-current areas (<10cm/s), current speed did not influence surface-canopy area, and surface-canopy area decreased by an average (mean $\pm$ sd) of 22.5 $\pm$ 2.4%/m, regardless of species. Unlike *Macrocystis*, *Nereocystis* was found in both low and high current areas (>10cm/s) and as such *Nereocystis* surface canopy area decreased at a higher and more variable rate (30.5 $\pm$ 9.1%/m) when compared to *Macrocystis* alone (22.7 $\pm$ 2.8%/m). Overall, given our findings and those of others linking tidal and current effects with observed kelp extent, we recommend minimizing the range of tidal conditions over which temporal analysis are conducted, and incorporating an explicit understanding of the role of currents when comparing between sites. Morphological differences in the canopy structures of *Macrocystis* and *Nereocystis* affected the buoyancy of each structure at the water's surface, which played a key role in the relative magnitude of the kelp R_{0+} in the RE and NIR wavelengths with submerged structures having lower overall R_{0+} than emergent structures, but a higher relative R_{0+} in the RE than the NIR. Kelp was more likely to be submerged at the periphery of the bed, and overall, RE indices detected around 18% more

submerged surface-canopy, however the use of red-edge indices may also result in overestimation of surface-canopy area due to misclassification of shallow submerged benthic vegetation. Both NDRE and NDVI indices can be used to detect kelp canopy, however, the NDRE may detect an additional 18% of canopy area versus the NDVI due to the additional detection of submerged portions of kelp canopy.

4.0 Summary and Conclusions

The goal of this thesis was to understand how submersion of kelp canopy affects the above-water reflectance of surface-canopy forming kelps, with a focus on how submersion due to tides, currents, and morphology affect the estimation of surface-canopy area for both *Macrocystis pyrifera* and *Nereocystis luetkeana*. Hyperspectral data from controlled experiments were used to investigate the effects of submersion on the spectral signature of kelp, and *in situ* hyperspectral as well as multispectral UAV data from kelp beds on the Central Coast of British Columbia were used to characterize the spectral differences in surface-canopy structures for both *Nereocystis*

and *Macrocystis*, as well as how submersion by tides and currents affect the ability to estimate surface-canopy area.

In the first chapter, submersion experiments determined that when kelp is submerged, the NIR region of kelp spectra was strongly absorbed. However, the shorter RE wavelengths were not absorbed at the same rate and were used to detect submerged kelp deeper in the water column. These findings suggested that the use of RE wavelengths in kelp mapping may improve accuracy when mapping partially submerged kelp canopy or attempting to derive kelp biomass from remote sensing imagery. However, if the remote sensor is concerned about misclassifying submerged vegetation as surface-canopy, longer NIR wavelengths should be used to minimize detection of submerged kelp.

In the second chapter, multispectral imagery paired with *in situ* oceanographic data determined that kelp surface-canopy area at low-current sites (*Macrocystis*, *Nereocystis*, and mixed beds) decreased at similar rates to one another regardless of species, but kelp beds in sites with high-currents (here *Nereocystis* only) decreased, on average, at nearly twice the rate. As such, the rate of surface-canopy decrease with increase in tidal height was less predictable for *Nereocystis* than it was for *Macrocystis* and mixed beds. *In situ* hyperspectral data showed that differential morphology, and therefore buoyancy, between surface-canopy structures affects the above-water spectral signature of each structure. As such, multispectral UAV imagery showed 18% more surface-canopy when detected using NDRE instead of NDVI, regardless of species.

Together the results of this research contribute to a growing volume of knowledge on the remote sensing of surface-canopy forming kelps. While some of the results are specific to nearshore kelp beds on the British Columbia coast, many of the findings are pertinent to the remote sensing of kelp forests around the globe. The use of red-edge wavelengths provide an interesting

opportunity for the remote sensor to detect more kelp surface-canopy deeper in the water column, however we recommend that caution is exercised if doing so, because there is also an increased chance for false-positives in surface-canopy detection with the use of red-edge bands, especially at lower tidal heights in shallow nearshore areas.

5.0 References

Algina J, Oshima TC, Lin W-Y. **1994**. Type I Error Rates for Welch's Test and James's Second-Order Test Under Nonnormality and Inequality of Variance When There Are Two Groups. *Journal of Educational Statistics* **19**: 275–291.

Arafeh-Dalmau N, Montaño-Moctezuma G, Martínez JA, Beas-Luna R, Schoeman DS, Torres-Moye G. **2019**. Extreme Marine Heatwaves Alter Kelp Forest Community Near Its Equatorial Distribution Limit. *Frontiers in Marine Science* **6**: 1–18.

ASD. **2017**. Light Theory and Measurement Using the FieldSpec HandHeld 2 Portable Spectroradiometer.

Augenstein EW, Stow D, Hope A. **1991**. Evaluation of SPOT HRV-XS Data for Kelp Resource Inventories. *Photogrammetric Engineering and Remote Sensing* **57**: 501–509.

Barsi JA, Lee K, Kvaran G, Markham BL, Pedelty JA. **2014**. The Spectral Response of the Landsat-8 Operational Land Imager. *Remote Sensing* **6**: 10232–10251.

Bell TW, Allen JG, Cavanaugh KC, Siegel DA. **2020**. Three decades of variability in California's giant kelp forests from the Landsat satellites. *Remote Sensing of Environment* **238**: 110811.

Britton-Simmons K, Eckman JE, Duggins DO. **2008**. Effect of tidal currents and tidal stage on estimates of bed size in the kelp *Nereocystis luetkeana*. *Marine Ecology Progress Series* **355**: 95–105.

Burnett NP, Koehl MAR. **2017**. Pneumatocysts provide buoyancy with minimal effect on drag for kelp in wave-driven flow. *Journal of Experimental Marine Biology and Ecology* **497**: 1–10.

Burt JM, Tinker MT, Okamoto DK, Demes KW, Holmes K, Salomon AK. **2018**. Sudden collapse of a mesopredator reveals its complementary role in mediating rocky reef regime shifts. *Proceedings of the Royal Society B: Biological Sciences* **285**: 20180553.

Butler C, Lucieer V, Wotherspoon S, Johnson C. **2020**. Multi-decadal decline in cover of giant kelp *Macrocystis pyrifera* at the southern limit of its Australian range. *Marine Ecology Progress Series* **653**: 1–18.

Byers SC, Mills EL, Stewart PL. **1978**. A comparison of methods of determining organic carbon in marine sediments, with suggestions for a standard method. *Hydrobiologia* **58**: 43–47.

Cavanaugh KC, Bell T, Costa M, Eddy NE, Gendall L, Gleason MG, Hessing-Lewis M, Martone R, McPherson M, Pontier O, *et al.* 2021a. A Review of the Opportunities and Challenges for Using Remote Sensing for Management of Surface-Canopy Forming Kelps. *Frontiers in Marine Science* **8**: 1536.

Cavanaugh KC, Cavanaugh KC, Bell TW, Hockridge EG. **2021b**. An Automated Method for Mapping Giant Kelp Canopy Dynamics from UAV. *Frontiers in Environmental Science* **8**: 587354.

Cavanaugh K, Siegel D, Kinlan B, Reed D. **2010**. Scaling giant kelp field measurements to regional scales using satellite observations. *Marine Ecology Progress Series* **403**: 13–27.

Cavanaugh K, Siegel D, Reed D, Dennison P. **2011**. Environmental controls of giant-kelp biomass in the Santa Barbara Channel, California. *Marine Ecology Progress Series* **429**: 1–17.

Cohen J. **1988**. *Statistical Power Analysis for the Behavioral Sciences*. New York: Routledge.

Coleman LJM, Martone PT. **2020**. Morphological plasticity in the kelp Nereocystis luetkeana (Phaeophyceae) is sensitive to the magnitude, direction, and location of mechanical loading. *Journal of Phycology* **56**: 1414–1427.

Dekker AG, Brando VE, Anstee JM. **2005**. Retrospective seagrass change detection in a shallow coastal tidal Australian lake. *Remote Sensing of Environment* **97**: 415–433.

Dierssen HM, Chlus A, Russell B. **2015**. Hyperspectral discrimination of floating mats of seagrass wrack and the macroalgae Sargassum in coastal waters of Greater Florida Bay using airborne remote sensing. *Remote Sensing of Environment* **167**: 247–258.

DJI. **2019**. Phantom 4 Multispectral User Manual [V1.0].

Druehl LD. **1970**. The pattern of Laminariales distribution in the northeast Pacific. *Phycologia* **9**: 237–247.

Druehl LD. **1978**. The distribution of Macrocystis integrifolia in British Columbia as related to environmental parameters. *Canadian Journal of Botany* **56**: 69–79.

Druehl LD, Clarkston B. **2016**. *Pacific Seaweeds: Updated and Expanded Edition*. Harbour Publishing.

Druehl LD, Wheeler WN. **1986**. Population biology of *Macrocystis integrifolia* from British Columbia, Canada. *Marine Biology* **90**: 173–179.

Duggins DO, Simenstad CA, Estes JA. **1989**. Magnification of Secondary Production by Kelp Detritus in Coastal Marine Ecosystems. *Science* **245**: 170–173.

Duncan MJ. **1973**. In situ studies of growth and pigmentation of the phaeophyceanNereocystis luetkeana. *Helgoländer Wissenschaftliche Meeresuntersuchungen* **24**: 510–525.

Faraway JJ. **2002**. *Practical Regression and Anova using R*. Bath: University of Bath.

Filella I, Penuelas J. **1994**. The red edge position and shape as indicators of plant chlorophyll content, biomass and hydric status. *International Journal of Remote Sensing* **15**: 1459–1470.

Finger DJI, McPherson ML, Houskeeper HF, Kudela RM. **2021**. Mapping bull kelp canopy in northern California using Landsat to enable long-term monitoring. *Remote Sensing of Environment* **254**: 112243.

Forrester WD. **1983**. *Canadian tidal manual*. Ottawa: Dept. of Fisheries and Oceans.

Giannini F, Hunt BPV, Jacoby D, Costa M. **2021**. Performance of OLCI Sentinel-3A satellite in the Northeast Pacific coastal waters. *Remote Sensing of Environment* **256**: 112317.

Gitelson AA, Kaufman YJ, Merzlyak MN. **1996**. Use of a green channel in remote sensing of global vegetation from EOS-MODIS. *Remote Sensing of Environment* **58**: 289–298.

Gower JFR, Doerffer R, Borstad GA. **1999**. Interpretation of the 685nm peak in water-leaving radiance spectra in terms of fluorescence, absorption and scattering, and its observation by MERIS. *International Journal of Remote Sensing* **20**: 1771–1786.

Hamilton SL, Bell TW, Watson JR, Grorud-Colvert KA, Menge BA. **2020**. Remote sensing: generation of long-term kelp bed data sets for evaluation of impacts of climatic variation. *Ecology* **101**: e03031.

Han L, Rundquist DC. **2003**. The spectral responses of *Ceratophyllum demersum* at varying depths in an experimental tank. *International Journal of Remote Sensing* **24**: 859–864.

Heiri O, Lotter AF, Lemcke G. **2001**. Loss on ignition as a method for estimating organic and carbonate content in sediments: reproducibility and comparability of results. *Journal of Paleolimnology* **25**: 101–110.

Hooker SB, Maritorena S. **2000**. An Evaluation of Oceanographic Radiometers and Deployment Methodologies. *Journal of Atmospheric and Oceanic Technology* **17**: 811–830.

Hu L, Hu C, Ming-Xia H. **2017**. Remote estimation of biomass of Ulva prolifera macroalgae in the Yellow Sea. *Remote Sensing of Environment* **192**: 217–227.

Jackson GA. **1984**. Internal Wave Attenuation by Coastal Kelp Stands. *Journal of Physical Oceanography* **14**: 1300–1306.

Jackson JM, Thompson RE, Brown LN, Willis PG, Borstad GA. **2015**. Satellite chlorophyll off the British Columbia Coast, 1997–2010. *Journal of Geophysical Research: Oceans*: 4709–4728.

Jenks GF. **1977**. *Optimal Data Classification For Choropleth Maps*. University of Kansas.

Jensen JR. **1980**. Remote Sensing Techniques for Kelp Surveys. *Photogrammetric Engineering and Remote Sensing* **46**: 743–755.

Kain JM. **1987**. Patterns of Relative Growth in *Nereocystis Luetkeana* (Phaeophyta). *Journal of Phycology* **23**: 181–187.

Karpouzli E, Malthus T. **2003**. The empirical line method for the atmospheric correction of IKONOS imagery. *International Journal of Remote Sensing* **24**: 1143–1150.

Kearney MS, Stutzer D, Turpie K, Stevenson JC. **2009**. The Effects of Tidal Inundation on the Reflectance Characteristics of Coastal Marsh Vegetation. *Journal of Coastal Research* **256**: 1177–1186.

Knipling EB. **1970**. Physical and physiological basis for the reflectance of visible and near-infrared radiation from vegetation. *Remote Sensing of Environment* **1**: 155–159.

Koehl MAR, Silk WK, Liang H, Mahadevan L. **2008**. How kelp produce blade shapes suited to different flow regimes: A new wrinkle. *Integrative and Comparative Biology* **48**: 834–851.

Krumhansl KA, Okamoto DK, Rassweiler A, Novak M, Bolton JJ, Cavanaugh KC, Connell SD, Johnson CR, Konar B, Ling SD, *et al.* 2016. Global patterns of kelp forest change over the past half-century. *Proceedings of the National Academy of Sciences* **113**: 13785–13790.

Krumhansl KA, Scheibling R. **2012**. Production and fate of kelp detritus. *Marine Ecology Progress Series* **467**: 281–302.

Kutser T. **2009**. Passive optical remote sensing of cyanobacteria and other intense phytoplankton blooms in coastal and inland waters. *International Journal of Remote Sensing* **30**: 4401–4425.

Kutser T, Vahtmäe E, Paavel B, Kauer T. **2013**. Removing glint effects from field radiometry data measured in optically complex coastal and inland waters. *Remote Sensing of Environment* **133**: 85–89.

Liew OW, Chong PCJ, Li B, Asundi AK. **2008**. Signature Optical Cues: Emerging Technologies for Monitoring Plant Health. *Sensors* **8**: 3205–3239.

Loos EA, Costa M. **2010**. Inherent optical properties and optical mass classification of the waters of the Strait of Georgia, British Columbia, Canada. *Progress in Oceanography* **87**: 144–156.

Lu Y, Li L, Hu C, Li L, Zhang M, Sun S, Lv C. **2016**. Sunlight induced chlorophyll fluorescence in the near-infrared spectral region in natural waters: Interpretation of the narrow reflectance peak around 761 nm. *Journal of Geophysical Research: Oceans* **121**: 5017–5029.

Mann KH. **1973**. Seaweeds: Their Productivity and Strategy for Growth. *Science* **182**: 975–981.

Maxar. **2020**. WorldView-3, Avalaible at https://resources.maxar.com/data-sheets/worldview-3.

Meroni M, Rossini M, Guanter L, Alonso L, Rascher U, Colombo R, Moreno J. **2009**. Remote sensing of solar-induced chlorophyll fluorescence: Review of methods and applications. *Remote Sensing of Environment* **113**: 2037–2051.

Micasense. **2019**. RedEdge-MX - MicaSense.

Mobley CD. **1994**. *Light and water: radiative transfer in natural waters*. San Diego: Academic Press.

Mobley CD. **1999**. Estimation of the remote-sensing reflectance from above-surface measurements. *Applied Optics* **38**: 7442–7455.

Mora-Soto A, Palacios M, Macaya EC, Gómez I, Huovinen P, Pérez-Matus A, Young M, Golding N, Toro M, Yaqub M, *et al.* 2020. A High-Resolution Global Map of Giant Kelp (*Macrocystis pyrifera*) Forests and Intertidal Green Algae (Ulvophyceae) with Sentinel-2 Imagery. *Remote Sensing* **12**.

Morel A, Prieur L. **1977**. Analysis of variations in ocean color. *Limnology and Oceanography* **22**: 709–722.

Mork M. **1996**. The effect of kelp in wave damping. *Sarsia* **80**: 323–327.

Mount R. **2005**. Acquisition of Through-water Aerial Survey Images.

Murray C, Markager S, Stedmon CA, Juul-Pedersen T, Sejr MK, Bruhn A. **2015**. The influence of glacial melt water on bio-optical properties in two contrasting Greenlandic fjords. *Estuarine, Coastal and Shelf Science* **163**: 72–83.

Mutanga O, Skidmore AK. **2004**. Hyperspectral band depth analysis for a better estimation of grass biomass (Cenchrus ciliaris) measured under controlled laboratory conditions. *International Journal of Applied Earth Observation and Geoinformation* **5**: 87–96.

Nahirnick NK, Hunter P, Costa M, Schroeder S, Sharma T. **2019a**. Benefits and Challenges of UAS Imagery for Eelgrass (Zostera marina) Mapping in Small Estuaries of the Canadian West Coast. *Journal of Coastal Research* **35**: 673.

Nahirnick NK, Reshitnyk L, Campbell M, Hessing-Lewis M, Costa M, Yakimishyn J, Lee L. **2019b**. Mapping with confidence; delineating seagrass habitats using Unoccupied Aerial Systems (UAS). *Remote Sensing in Ecology and Conservation* **5**: 121–135.

Nicholson NL. **1970**. Field Studies on the Giant Kelp *Nereocystis*. *Journal of Phycology* **6**: 177–182.

Nicholson NL. **1976**. Anatomy of the Medulla of *Nereocystis*. *Botanica Marina* **19**: 23–31.

Nicholson NL, Briggs WR. **1972**. TRANSLOCATION OF PHOTOSYNTHATE IN THE BROWN ALGA *NEREOCYSTIS*. *American Journal of Botany* **59**: 97–106.

Nijland W, Reshitnyk L, Rubidge E. **2019**. Satellite remote sensing of canopy-forming kelp on a complex coastline: A novel procedure using the Landsat image archive. *Remote Sensing of Environment* **220**: 41–50.

Olmedo-Masat OM, Raffo MP, Rodríguez-Pérez D, Arijón M, Sánchez-Carnero N. **2020**. How Far Can We Classify Macroalgae Remotely? An Example Using a New Spectral Library of Species from the South West Atlantic (Argentine Patagonia). *Remote Sensing* **12**: 3870.

Olson AM, Hessing-Lewis M, Haggarty D, Juanes F. **2019**. Nearshore seascape connectivity enhances seagrass meadow nursery function. *Ecological Applications* **29**: e01897.

O'Neill JD. **2006**. Mapping of Eelgrass (*Zostera marina*) at Sidney Spit, Gulf Islands National Park Reserve of Canada, Using High Spatial Resolution Remote Imagery. M.Sc. Thesis, University of Victoria, Victoria, BC, Canada, 2010.

O'Neill JD, Costa M. **2013**. Mapping eelgrass (*Zostera marina*) in the Gulf Islands National Park Reserve of Canada using high spatial resolution satellite and airborne imagery. *Remote Sensing of Environment* **133**: 152–167.

O'Neill JD, Costa M, Sharma T. **2011**. Remote Sensing of Shallow Coastal Benthic Substrates: In situ Spectra and Mapping of Eelgrass (Zostera marina) in the Gulf Islands National Park Reserve of Canada. *Remote Sensing* **3**: 975–1005.

Pegau WS, Gray D, Zaneveld JRV. **1997**. Absorption and attenuation of visible and near-infrared light in water: dependence on temperature and salinity. *Applied Optics* **36**: 6035–6046.

Pfister CA, Berry HD, Mumford T. **2017**. The dynamics of Kelp Forests in the Northeast Pacific Ocean and the relationship with environmental drivers (A Randall Hughes, Ed.). *Journal of Ecology* **106**: 1520–1533.

Phillips SR, Costa M. **2017**. Spatial-temporal bio-optical classification of dynamic semi-estuarine waters in western North America. *Estuarine, Coastal and Shelf Science* **199**: 35–48.

Preisendorfer RW. **1986**. Secchi disk science: Visual optics of natural waters. *Limnology and Oceanography* **31**: 909–926.

RD Instruments. **2005**. RDI ADCP WorkHorse Technical Manual- April 2005.pdf.

Ritchie JC, Zimba PV, Everitt JH. **2003**. Remote Sensing Techniques to Assess Water Quality. *Photogrammetric Engineering & Remote Sensing* **69**: 695–704.

Roesler CS, Perry MJ. **1995**. In situ phytoplankton absorption, fluorescence emission, and particulate backscattering spectra determined from reflectance. *Journal of Geophysical Research: Oceans* **100**: 13279–13294.

Rogers-Bennett L, Catton CA. **2019**. Marine heat wave and multiple stressors tip bull kelp forest to sea urchin barrens. *Scientific Reports* **9**: 15050.

Rouse W, Haas RH, Deering W. **1974**. *MONITORING THE VERNAL ADVANCEMENT AND RETROGRADATION (GREEN WAVE EFFECT) OF NATURAL VEGETATION*. Greenbelt, Md.: Goddard Space Flight Center.

Ruru D, Yingqing H, Yan Q, Qidong C, Lei C. **2012**. Measuring pure water absorption coefficient in the near-infrared. *Journal of Remote Sensing* **16**: 192–206.

Sathyendranath S, Lazzara L, Prieur L. **1987**. Variations in the spectral values of specific absorption of phytoplankton. *Limnology and Oceanography* **32**: 403–415.

Satlantic. **2012**. Profiler II Operation Manual SAT-DN-00223 revK.pdf.

Schalles JF, Gitelson AA, Yacobi YZ, Kroenke AE. **1998**. ESTIMATION OF CHLOROPHYLL a FROM TIME SERIES MEASUREMENTS OF HIGH SPECTRAL RESOLUTION REFLECTANCE IN AN EUTROPHIC LAKE. *Journal of Phycology* **34**: 383–390.

Schmitz K, Srivastava LM. **1976**. THE FINE STRUCTURE OF SIEVE ELEMENTS OF NEREOCYSTIS LÜTKEANA. *American Journal of Botany* **63**: 679–693.

Schroeder SB, Boyer L, Juanes F, Costa M. **2019a**. Spatial and temporal persistence of nearshore kelp beds on the west coast of British Columbia, Canada using satellite remote sensing. *Remote Sensing in Ecology and Conservation* **6**: 327–343.

Schroeder SB, Dupont C, Boyer L, Juanes F, Costa M. **2019b**. Passive remote sensing technology for mapping bull kelp (Nereocystis luetkeana): A review of techniques and regional case study. *Global Ecology and Conservation* **19**: e00683.

Schultz BB. **1985**. Levene's Test for Relative Variation. *Systematic Biology* **34**: 449–456.

Shaffer JA. **2000**. Seasonal Variation in Understory Kelp Bed Habitats of the Strait of Juan de Fuca. *Journal of Coastal Research* **16**: 768–775.

Shingala MC, Rajyaguru DA. **2015**. Comparison of Post Hoc Tests for Unequal Variance. *International Journal of New Technologies in Science and Engineering* **2**: 12.

Slaton MR, Hunt ER, Smith WK. **2001**. Estimating Near-Infrared Leaf Reflectance from Leaf Structural Characteristics. *American Journal of Botany* **88**: 278–284.

Song B, Park K. **2020**. Detection of Aquatic Plants Using Multispectral UAV Imagery and Vegetation Index. *Remote Sensing* **12**: 387.

Springer Y, Hays C, Carr MH, Mackey M. **2007**. *ECOLOGY and MANAGEMENT of the BULL KELP, NEREOCYSTIS LUETKEANA: A Synthesis with Recommendations for Future Research*. Lenfest Ocean Program.

Stekoll MS, Deysher LE, Hess M. **2006**. A remote sensing approach to estimating harvestable kelp biomass. *Journal of Applied Phycology* **18**: 323–334.

Stine RA. **1995**. Graphical Interpretation of Variance Inflation Factors. *The American Statistician* **49**: 53–56.

Sutherland IR. **1990**. *Kelp Inventory, 1989 The Vancouver Island and Malcolm Island Shores of Queen Charlotte Strait Including a summary of historical inventory information for the area*. Ministry of Environment.

Sutherland IR. **2008**. *Kelp inventory, 2007 : areas of the British Columbia Central Coast from Hakai Passage to the Bardswell Group*. Ministry of Environment, Canada.

Tegner MJ, Dayton PK. **1987**. El Nino Effects on Southern California Kelp Forest Communities. *Advances in Ecological Research* **17**: 243–279.

Thomson RE. **1981**. *Oceanography of the British Columbia coast*. Ottawa: Dept. of Fisheries and Oceans.

Tucker CJ. **1978**. A Comparison of Satellite Sensor Bands for Vegetation Monitoring. *Photogrammetric Engineering and Remote Sensing* **44**: 1369–1380.

Tucker CJ. **1979**. Red and Photographic Infrared linear Combinations for Monitoring Vegetation. *Remote Sensing of Environment* **8**: 127–150.

Turpie KR. **2013**. Explaining the Spectral Red-Edge Features of Inundated Marsh Vegetation. *Journal of Coastal Research* **290**: 1111–1117.

Vahtmäe E, Paavel B, Kutser T. **2020**. How much benthic information can be retrieved with hyperspectral sensor from the optically complex coastal waters? *Journal of Applied Remote Sensing* **14**: 016504.

Valle-Levinson A, Daly MA, Juarez B, Tenorio-Fernandez L, Fagundes M, Woodson CB, Monismith SG. **2022**. Influence of kelp forests on flow around headlands. *Science of The Total Environment* **825**: 153952.

Welch BL. **1947**. The Generalization of `Student's' Problem when Several Different Population Variances are Involved. *Biometrika* **34**: 28–35.

Wernberg T, Krumhansl K, Filbee-Dexter K, Pedersen MF. **2019**. Status and Trends for the World's Kelp Forests. In: World Seas: an Environmental Evaluation. Elsevier, 57–78.

Wheeler WN. **1980**. Pigment content and photosynthetic rate of the fronds of Macrocystis pyrifera. *Marine Biology* **56**: 97–102.

Wheeler WN, Smith RG, Srivastava LM. **1984**. Seasonal photosynthetic performance of *Nereocystis luetkeana*. *Canadian Journal of Botany* **62**: 664–670.

Wyatt B, Burt WV, Pattullo JG. **1972**. Surface Currents off Oregon as Determined from Drift Bottle Returns. *Journal of Physical Oceanography* **2**: 286–293.